Topological nanomaterials

Pengzi Liu[1,2], *James R. Williams*[3,4]* *and Judy J. Cha*[1,2,5]*

Abstract | The past decade has witnessed the emergence of a new frontier in condensed matter physics: topological materials with an electronic band structure belonging to a different topological class from that of ordinary insulators and metals. This non-trivial band topology gives rise to robust, spin-polarized electronic states with linear energy–momentum dispersion at the edge or surface of the materials. For topological materials to be useful in electronic devices, precise control and accurate detection of the topological states must be achieved in nanostructures, which can enhance the topological states because of their large surface-to-volume ratios. In this Review, we discuss notable synthesis and electron transport results of topological nanomaterials, from topological insulator nanoribbons and plates to topological crystalline insulator nanowires and Weyl and Dirac semimetal nanobelts. We also survey superconductivity in topological nanowires, a nanostructure platform that might enable the controlled creation of Majorana bound states for robust quantum computations. Two material systems that can host Majorana bound states are compared: spin–orbit coupled semiconducting nanowires and topological insulating nanowires, a focus of this Review. Finally, we consider the materials and measurement challenges that must be overcome before topological nanomaterials can be used in next-generation electronic devices.

A decade has passed since the first experimental observation of topological materials that do not require stringent experimental conditions to realize a topological state[1]. Topological materials are characterized by an electronic band structure that exhibits a special band topology[2–4], which is now essential to understand the physical properties of many materials. These materials possess topologically protected surface states with unique electronic properties; in topological insulators (TIs), the surface states arise from the inversion of the bulk bandgap, which is induced by the large spin–orbit coupling of the heavy atoms in the material, and are protected by time-reversal symmetry. In topological crystalline insulators (TCIs), the surface states are protected by crystal symmetry instead. In recent years, topological materials have expanded to include topological semimetals: Weyl and Dirac semimetals[5] are 3D systems that possess gapless bulk states in the form of relativistic chiral fermions near nodal points and Fermi arc surface states, and are described by the 3D Weyl and Dirac[6] equations, respectively. With breaking of symmetry, either inversion symmetry or time-reversal symmetry, a Dirac semimetal can become a Weyl semimetal, as each Dirac point splits into a pair of Weyl points. The early development of topological materials, including notable experimental results and theoretical background on TIs[7–16], TCIs[17,18] and topological semimetals[5], is covered in several review articles[5,19–23].

The electronic properties of the topologically protected surface states are attractive for future electronic applications. For example, the linear dispersion between momentum and energy is promising for high-speed electronics[24–26], the locking of spin and momentum for spintronics[27–31] and the helical nature of the electrons for low-dissipation electronics (in which helical means that the direction of motion of the electrons depends on their spin direction)[32–34]. The unique features of the topological surface states have been investigated extensively by using high-quality bulk crystals, thin films and surface-sensitive techniques. For example, the band structure and helical nature of the topological surface states have been directly visualized through angle-resolved photoemission spectroscopy (ARPES), hard X-ray photoelectron spectroscopy and momentum-resolved photoelectron microscopy on cleaved TIs[35–39]. Exotic condensed matter states, such as the quantum spin Hall state and the quantum anomalous Hall state, have also been realized with epitaxially grown thin films of topological materials[1,40–44]. These quantum states provide a rich playground in which to investigate fundamental interactions of correlated electrons under topological protection and can be exploited for applications. For device applications, topological materials in the form of nanostructures are necessary for integration into existing device fabrication technologies. In particular, thin-film topological materials are attractive,

[1]*Department of Mechanical Engineering and Materials Science, Yale University, New Haven, CT, USA.*

[2]*Energy Sciences Institute, Yale West Campus, West Haven, CT, USA.*

[3]*Department of Physics, University of Maryland, College Park, MD, USA.*

[4]*Joint Quantum Institute, University of Maryland, College Park, MD, USA.*

[5]*Canadian Institute for Advanced Research Azrieli Global Scholar, Toronto, ON, Canada.*

**e-mail: jwilliams@physics.umd.edu; judy.cha@yale.edu*

https://doi.org/10.1038/s41578-019-0113-4

because artificial, design-specific heterostructures that interface topological materials with other functional materials, such as superconductors or ferromagnetic insulators, can be fabricated with atomic precision[45–51]. Device applications that are being explored include topological field-effect transistors based on the quantum spin Hall state, which can be rapidly switched off and may be useful for low-power quantum electronics[52], low-power topological magnetic memory devices that exploit the spin-polarized topological surface current[53] and perhaps most excitingly robust quantum bits (qubits) that do not suffer from decoherence[4]. All proposed device applications rely on nanostructures of topological materials.

Studying topological surface states in nanostructures has the advantage that nanostructures reduce as much as possible the influence of the undesirable bulk electronic states in transport measurements, while increasing the surface-to-volume ratio to enhance the contribution of the topological surface or edge states. In early studies of layered TIs, such as Bi_2Se_3 and Bi_2Te_3, mechanical exfoliation was used to obtain thin flakes from bulk crystals to maximize the effects of the surface states. Direct synthesis of topological nanomaterials has advanced research into topological states of matter. Transport experiments were performed on TI and TCI nanostructures grown by the vapour–liquid–solid (VLS) and chemical vapour deposition (CVD) methods (BOX 1). Additional advantages of topological nanostructures for studying topological surface states include the possibility of using effective field-effect gating to tune the Fermi level, potentially adapting the wrap-around gate architecture to the topological nanowires; engineering the bulk bandgap and sub-bands by exploiting the nanoscale confinement; and realizing new correlated electronic states due to quantum confinement, leading to phenomena such as the unexpected ballistic transport observed in $LaAlO_3/SrTiO_3$ quantum wires[54,55].

The nanowire geometry is particularly suitable for nanoelectronic device measurements, such as measurements of the Aharonov–Bohm oscillations (oscillations in the resistance as a function of the magnetic flux). Aharonov–Bohm oscillation studies allow phase-sensitive transport measurements of the topological surface states, which are made possible by the well-defined nanoscale cross-section of the samples. The Aharonov–Bohm oscillations have been observed in several topological nanowire systems, such as Bi_2Se_3 and Bi_2Te_3 TI nanoribbons and nanotubes[56–59], SnTe TCI nanowires[60] and more recently Cd_3As_2 topological semimetal nanowires[61].

Finally, one of the most compelling reasons to study topological nanomaterials is the potential realization of 1D topological superconductors by using TI and TCI nanowires with diameters between ~10 nm and ~200 nm and lengths of more than tens of micrometres. Superconducting TI or TCI nanowires are predicted to host Majorana bound states (MBSs) — quasiparticle excitations that are identical to their antiparticle counterparts[62] — which can be exploited for fault-tolerant and scalable topological quantum computations without decoherence[63].

In this Review, we survey recent work on TI, TCI, and Weyl and Dirac semimetal nanostructures, grown primarily by the VLS and CVD methods, highlighting notable synthesis and transport measurements. We then focus on the control offered by TI nanowires for realizing 1D topological superconductivity to create MBSs and compare them to another material system that can host MBSs: semiconductor nanowires with strong spin–orbit coupling[64]. To demonstrate the benefits of TI nanowires, we present numerical simulations that demonstrate local control of the topological superconducting state using a TI nanowire. Finally, we discuss remaining challenges in realizing topological nanostructures with high crystal quality and precise morphology control, and in growing robust topological superconducting nanowires.

Synthesis of topological nanomaterials

Most TIs and TCIs and some topological semimetals have been made into nanostructures, either by mechanical exfoliation from bulk layered crystals or by direct synthesis. This section focuses on the direct synthesis of topological nanomaterials. VLS and CVD growth methods (BOX 1) are the two most broadly used methods for the synthesis of topological nanostructures used to study electrical transport properties. A chronological summary of the synthesis milestones of topological nanomaterials made of TIs, TCIs, and Weyl and Dirac semimetals is presented in FIG. 1.

TI nanostructures. Following the prediction that some binary chalcogenides are 3D TIs[7], Bi_2Se_3, Bi_2Te_3, Sb_2Te_3 and their alloys were quickly synthesized as nanoribbons and nanoplates by the VLS and CVD growth methods[56,65,66] (FIG. 2a). Before this prediction, the binary chalcogenides had been extensively studied for their thermoelectric properties and have been made into a variety of nanostructures, including nanorods[67], nanotubes[68], nanosheets, nanospheres[69] and nanoplates[70].

Bi_2Se_3 nanoribbons were first synthesized by metal-catalysed CVD[71]. Gold nanoparticles were used to catalyse the growth, and Bi_2Se_3 source powder was heated to form the vapour. The widths of the nanoribbons were larger than the size of the gold nanoparticles, suggesting that the growth mechanism was a combination of VLS and CVD. Without the use of metal catalysts, Bi_2Te_3 nanoplates with thicknesses ranging from a few quintuple layers to tens of nanometres were grown by CVD[65]. Because Bi_2Se_3 and Bi_2Te_3 are layered, large nanoplates can be easily obtained by CVD. Ternary compounds, such as $(Bi_xSb_{1-x})_2Te_3$ and $Bi_2(Se_xTe_{1-x})_3$, have also been grown by mixing two binary source powders[72,73]. Doping of TI nanomaterials has also been demonstrated[74–79]: Bi_2Se_3 nanoribbons have been doped magnetically by using Fe metal catalysts or introducing ferrocene vapour during growth[74]. Doping Bi_2Se_3 nanoribbons with Sb has proved effective in achieving a low carrier density of 2×10^{11} cm^{-2} (REF.[77]). To reduce the bulk carrier density, which is key to maximizing the contribution from the topological surface states to the transport signal, the ideal approach would be to eliminate intrinsic chalcogen vacancies. However, it is unclear how easy it is to achieve this goal with the VLS or CVD growth methods. As an

Box 1 | **Vapour–liquid–solid and chemical vapour deposition growth**

The two most popular growth techniques for synthesizing topological nanomaterials are the vapour–liquid–solid (VLS) and chemical vapour deposition (CVD) methods. VLS growth is a metal-catalysed nanowire growth method, which was first demonstrated to grow Si microwires[183]. In VLS growth, metal nanoparticles, typically gold, are used to catalyse growth, and the source materials are introduced as vapour. At growth temperature, the metal catalyst is in the liquid state, and the gas molecules or atoms of the source material dissolve into the liquid metal particle. When the concentration of the source atoms in the liquid metal exceeds the thermodynamic solubility limit at the given growth temperature, the dissolved source atoms precipitate and form a crystalline solid at one end of the liquid metal particle. With continual supply of source vapour, an equilibrium is reached in which the metal particle maintains the solubility limit concentration by ejecting the excess dissolved atoms, lengthening the nanowire. A distinguishing feature of the VLS growth is that the diameter of the nanowire is precisely determined by the size of the metal nanoparticle[184]. This growth technique is widely used to obtain semiconducting nanowires, as well as heterostructure and core–shell nanowires[185–187] for applications including field-effect transistors, solar cells, nanolasers, biosensors and thermoelectrics.

In CVD growth, gaseous source materials are deposited on a growth substrate to obtain thin films, microcrystals or nanostructures. The source materials can be introduced directly as vapour or can be vaporized by heating solid powders. The source vapours are usually carried down to the substrate (which is kept at a lower temperature than the vapour) by an inert carrier gas, and there they condense to form solid thin films or nanocrystals. If different source vapours are mixed, they may react with each other before condensing to form solids. Many 2D materials, such as graphene, hexagonal boron nitride and transition metal dichalcogenides, have been grown by CVD[165,188,189]. Topological nanostructures are often grown using metal-catalysed CVD, which uses metal nanoparticles as nucleation catalysts. Unlike in VLS, in metal-catalysed CVD the width of the nanostructure is often much larger than the size of the metal nanoparticle.

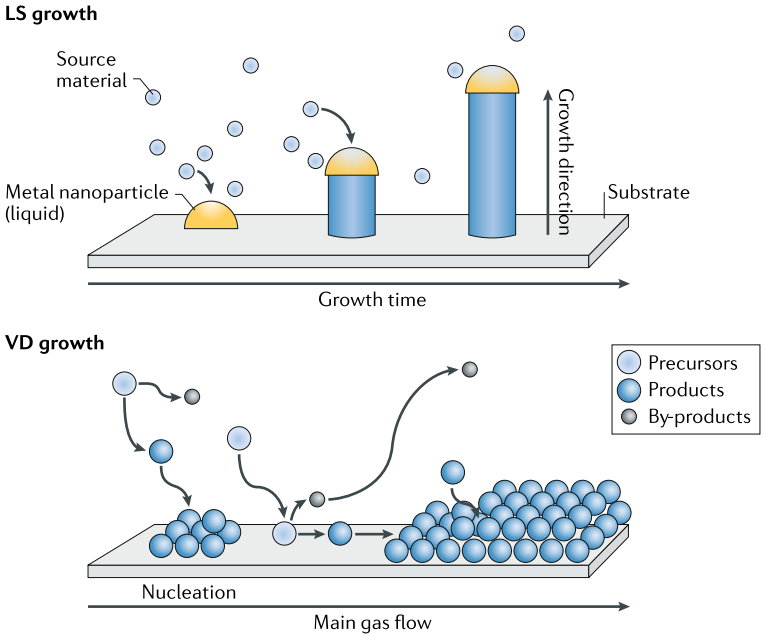

alternative, doping studies that explore different dopants and dopant concentrations should be carried out for TI nanostructures.

TCI nanostructures. Whereas TIs are protected by time-reversal symmetry and possess a single topological surface Dirac cone (for the binary chalcogenides), TCIs are protected by a crystal-symmetry invariant[80] and possess multiple topological surface Dirac cones. The TCI SnTe was grown as nanowires, nanoplates and microcrystals through CVD[60,81] (FIG. 2a). Unlike the 3D TIs, which have a layered crystal structure, SnTe is cubic. Thus, cubic nanocrystals or nanowires with square cross-sections are expected. However, metal-catalysed CVD can produce large SnTe nanoplates with nanometre thickness and a lateral dimension on the micrometre scale. The use of metal catalysts and choice of growth substrates greatly affect the morphology of TCI nanostructures. Without the use of gold nanoparticles, cubic SnTe microcrystals were grown on SiO_2/Si substrates[81]. Systematic growths of SnTe and its alloy nanostructures on various amorphous and crystalline substrates were performed[82–85], and indicated that the strength of the interaction between the growth substrate and the surface adatoms can dictate the morphology of TCI nanostructures and the growth direction of TCI nanoplates; that is, whether TCI nanoplates grow standing vertically, with minimum contact with the substrate, or lying flat, maximizing contact. The interaction strength also influences the diffusivity of the surface adatoms, controlling the growth kinetics of the nanostructures[84,85]. The morphology of SnTe microcrystals as a function of growth conditions was also investigated. It was found that the surface energies of different crystallographic planes can change with the local chemical potential of Sn or Te vapours[83], leading to different morphologies of SnTe microcrystals that minimize the total surface energy (FIG. 2b).

Additional TCI nanostructures, such as $Pb_xSn_{1-x}Te$, $Pb_xSn_{1-x}Se$, $In_xSn_{1-x}Te$ and $SnSe_xTe_{1-x}$ nanowires and nanoplates[84,86–88], have been grown to study the phase transition from a trivial to a non-trivial topological state as a function of Pb doping[84]; to induce superconductivity by using In dopants[89,90]; and to reduce the bulk carrier density by Se anion doping[91]. Doping was generally achieved by mixing dopant powders directly with source powders during CVD growth.

Weyl and Dirac semimetal nanostructures. For the most part, Weyl and Dirac semimetals have been studied using bulk crystals, such as TaAs, TaP (REFS[92,93]), NbAs (REF.[94]) and NbP crystals[95]. Mechanical exfoliation to obtain nanostructures is generally tricky, as many of the topological semimetals are not layered crystals. For nanostructures, type II Weyl semimetal $MoTe_2$ in the polymorph structure 1T′ was synthesized as few-layer films and flakes by CVD[96,97], and 1T′-WTe_2 as nanoribbons and flakes[98,99]. The distinction between type I and type II Weyl semimetals is based on whether the Weyl point is point-like at the Fermi surface (type I) or the Weyl points appear as a line (type II)[100]. Type I Dirac semimetal Cd_3As_2 has been grown by CVD as nanobelts and nanowires[61] (FIG. 2c).

Compared with TI and TCI nanostructures, the direct synthesis of Weyl and Dirac semimetals into nanostructures is more challenging. For example, CVD growth of tellurium-based transition metal dichalcogenides is more difficult than CVD growth of sulfur-based and selenium-based transition metal dichalcogenides, owing to the low formation energies of Te-based compounds such as WTe_2. In addition, many Weyl and Dirac semimetals either contain toxic elements, such as arsenic, or involve precursors that can form toxic compounds, such as phosphorus. This makes the synthesis of nanostructures through simple VLS and CVD set-ups challenging

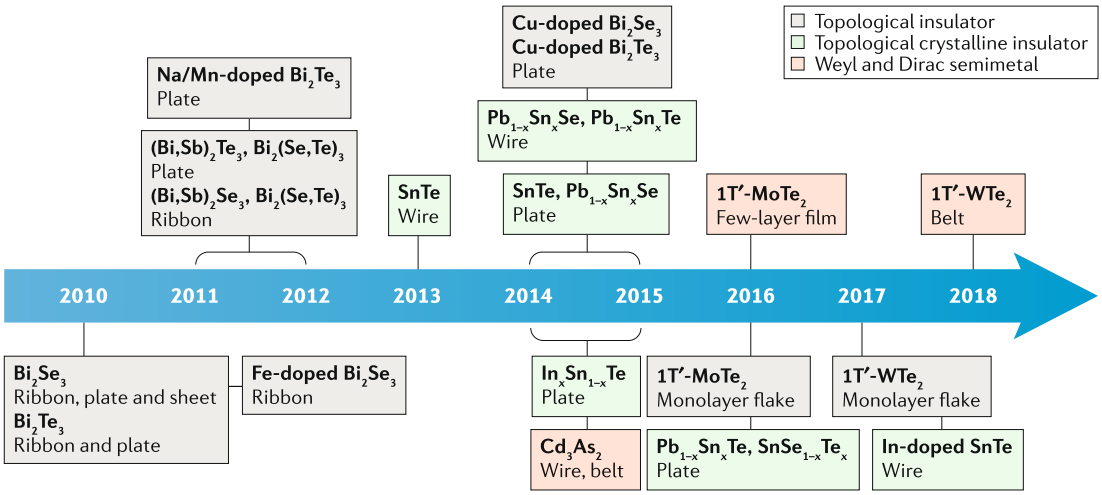

Fig. 1 | **Historical timeline of the synthesis of nanostructures of topological materials.** First synthesis of various topological materials as nanostructures obtained by vapour–liquid–solid and chemical vapour deposition growth methods.

for topological semimetals and creates a need for growth set-ups that can handle toxic gases.

Electron transport in topological nanostructures

The nature of the topological surface states in nanostructures was probed by measuring electron transport properties of nanodevices. Sufficient experimental results have been reported on TI and TCI nanostructures to confirm the presence of the expected topological surface states and their helical Dirac nature. They include ARPES measurements on TI nanoplates to visualize the topological surface state directly[101], electron transport measurements of TI and TCI nanodevices to demonstrate the 2D and helical nature of the surface states[13,16,102,103], and measurements using Josephson junction devices to study the nature of the superconductivity induced in TI nanostructures[104–107]. For Dirac and Weyl semimetals, surface transport has been inferred from quantum interference studies in Cd_3As_2, 1T′-$MoTe_2$ and 1T′-WTe_2 nanostructures[61,108–110].

This section reviews notable electron transport results for topological nanostructures; a chronological summary is presented in FIG. 3. Additional transport results on TI and TCI nanomaterials are summarized in dedicated reviews[111,112].

TI nanostructures. For TI nanoplate devices, a combination of doping, alloying and field-effect gating can be used to effectively control the Fermi level and minimize the residual bulk carrier density[65,72,73,84,89]. Ambipolar transport obtained by gating through conventional dielectric layers or an ionic liquid layer has been demonstrated in CVD-grown $(Bi_xSb_{1-x})_2Te_3$ nanoplates[72], $(Bi_xSb_{1-x})_2Se_3$ nanoribbons[77] and $(Bi_xSb_{1-x})_2Se_3$ nanoplates[113], and exfoliated Bi_2Se_3 nanoplates[114]. This is an important demonstration, because it shows that the Fermi level can be tuned through the Dirac cone and within the bulk gap, which ensures that only the topological surface states contribute to the transport signal.

Early transport studies of TI nanostructures focused on the weak antilocalization feature, which is linked to a quantum correction to the magnetoresistance due to the wave nature of the electrons in a diffusive regime. The feature appears as a dip in the magnetoresistance in small magnetic fields and can be fitted to 2D localization physics using the Hikami–Larkin–Nagaoka (HLN) equation[115] to infer the presence of the surface states[65,73,77,116,117]. However, localization physics in the diffusive transport regime is not ideal for probing the surface states, because scattering of electrons inevitably leads to the degradation of transport properties and loss of phase information. 2D Shubnikov–de Haas oscillations, oscillations in conductivity that reflect the quantum mechanical nature of electrons in the presence of large magnetic fields, were investigated to probe the nature of the Fermi surface in several TI nanoflakes exfoliated from bulk crystals[106,118]. Landau-level fan diagrams obtained from the oscillations were analysed to see if the intercept was −1/2, a signature of Dirac fermions. This analysis can be accurate only if the carrier density is low enough that the Landau indices are small[119]. In one Bi_2Se_3 nanoribbon study[120], the observed 2D Shubnikov–de Haas oscillations indicated a low carrier density of 1.3×10^{12} cm^{-2} for the surface state, placing the Fermi level within the bulk bandgap, at 95 meV below the bottom of the bulk conduction band. The helical nature of the topological surface state was inferred in exfoliated TI nanoflakes by generating a spin-polarized photocurrent with circularly polarized light[121].

Electron transport measurements that really exploit the nanoscale dimension of TI nanostructures are the Aharonov–Bohm oscillation studies on narrow nanoribbons or nanowires[56] (FIG. 4a). Aharonov–Bohm oscillations are a quantum interference effect produced by electrons encircling a magnetic flux and acquiring a Berry phase shift of π. This is manifested in the resistance, which oscillates as a function of magnetic field B with a periodicity of $\Phi_0 = h/e$ (conventional electrons) or $h/2e$ (helical electrons). The Aharonov–Bohm oscillations were first observed in Bi_2Se_3 nanoribbons and studied more carefully in follow-up experiments using Se-coated Bi_2Se_3 nanoribbons[57] (FIG. 4b–e).

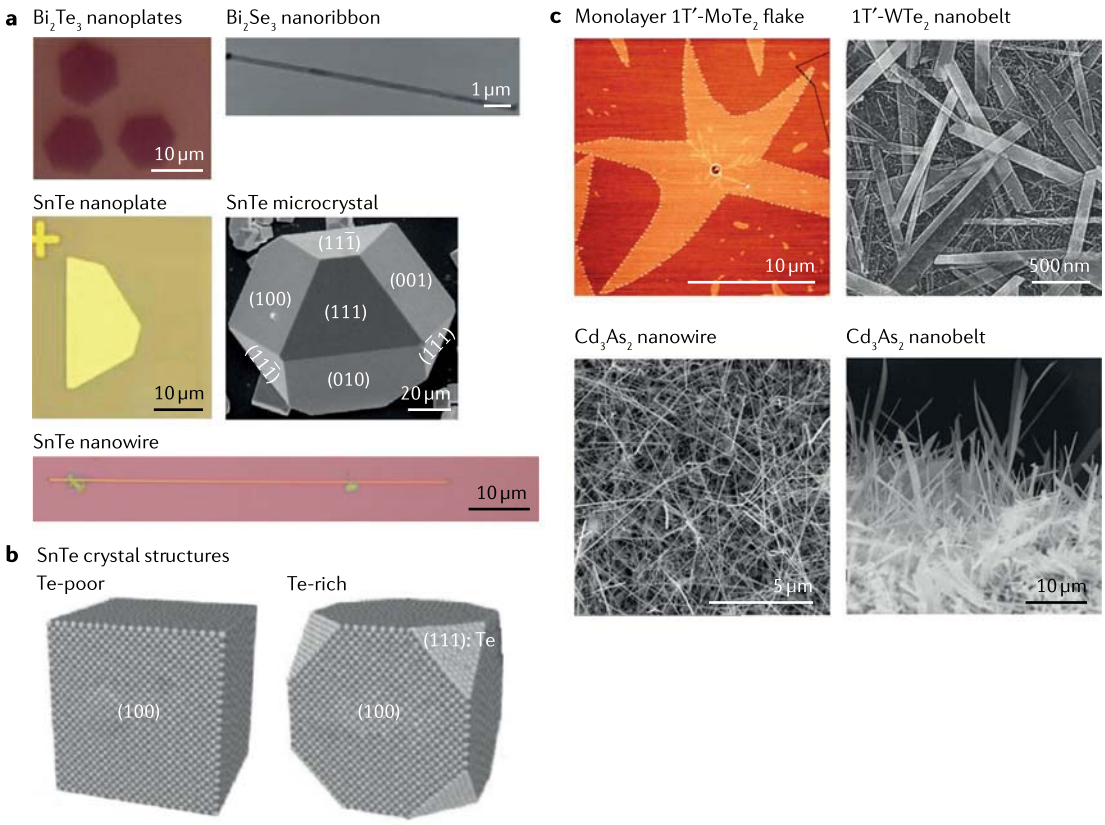

Fig. 2 | **Topological insulators, topological crystalline insulators, and Dirac and Weyl semimetallic nanostructures.** **a** | Topological insulator and topological crystalline insulator nanostructures: Bi_2Te_3 nanoplates, Bi_2Se_3 nanoribbon, SnTe nanoplate, SnTe microcrystal and SnTe nanowire synthesized using the vapour–liquid–solid and chemical vapour deposition (CVD) growth methods. **b** | Wulff constructions of the thermodynamic equilibrium SnTe crystals at Te-poor and Te-rich conditions. **c** | Dirac and Weyl semimetal nanostructures: a monolayer 1T′-$MoTe_2$ flake, 1T′-WTe_2 nanobelts, Cd_3As_2 nanowires and Cd_3As_2 nanobelts grown by CVD. Panel **a** is adapted with permission from REFS[65,170], ACS; REF.[56], Springer Nature Limited; REF.[128], CC-BY-4.0; and REF.[160], Elsevier. Panel **b** is adapted with permission from REF.[170], ACS. Panel **c** is reproduced with permission from REF.[97], ACS; REF.[98], Wiley-VCH; and REF.[191], RSC.

The Se coating was critical in preventing surface oxidation, which degrades the carrier mobility and introduces a low-mobility electron gas on the surface[122]. Careful analysis revealed that the oscillations did indeed originate from the topological surface electrons. Aharonov–Bohm oscillations with conductance maxima at odd values of $\Phi = \pm\Phi_0/2$ have been reproduced in Bi_2Te_3 nanoribbons (FIG. 4f) and nanotubes[58,59]. Aharonov–Bohm oscillations were also observed in SnTe TCI nanowires[60] and Cd_3As_2 topological semimetal nanowires[61].

TCI nanostructures. Soon after the experimental identification of SnTe and its alloys as TCIs by ARPES, SnTe and doped SnTe nanowires and nanoplates were synthesized and their electron transport properties investigated. Aharonov–Bohm oscillations, Shubnikov–de Haas oscillations and weak antilocalization have been observed in VLS-grown pristine or Pb-doped SnTe nanowires[60,88] (FIG. 4g). One main distinction between TIs and TCIs is the number of topological surface states in the system. The binary chalcogenide TIs possess one surface state, whereas the SnTe-based TCIs possess four surface states on each of the {001}, {111} and {110} surface planes[123]. In principle, information on the number of surface Dirac cones can be extracted from weak antilocalization measurements. The scaling parameter α in the HLN equation should reflect the number of cones present: a single Dirac cone would give $\alpha = -0.5$. For SnTe and its alloy nanoplates, values of $|\alpha|$ ranging from 0.5 to 5 have been reported, suggesting the presence of multiple Dirac cones[124]. However, a simple one-to-one correspondence between α and the number of cones is complicated by the presence of a conducting bulk. For example, even for TI nanostructures with a single Dirac cone, the value for α is often not −0.5 and depends on many factors. For TCI nanostructures with multiple Dirac cones, it is difficult to probe the surface states using weak antilocalization. One study suggests that the weak antilocalization observed in SnTe nanoplates is a bulk effect[89]. Aharonov–Bohm oscillations were reported in SnTe nanowires[60] (FIG. 4g), but there were no follow-up studies. More careful analysis of the Aharonov–Bohm oscillations is necessary to understand the nature of the multiple Dirac cones in SnTe, and this remains a problem in the field.

Another factor to consider for TCIs, which is absent in TIs, is the structural transition from the high-temperature cubic structure to the low-temperature

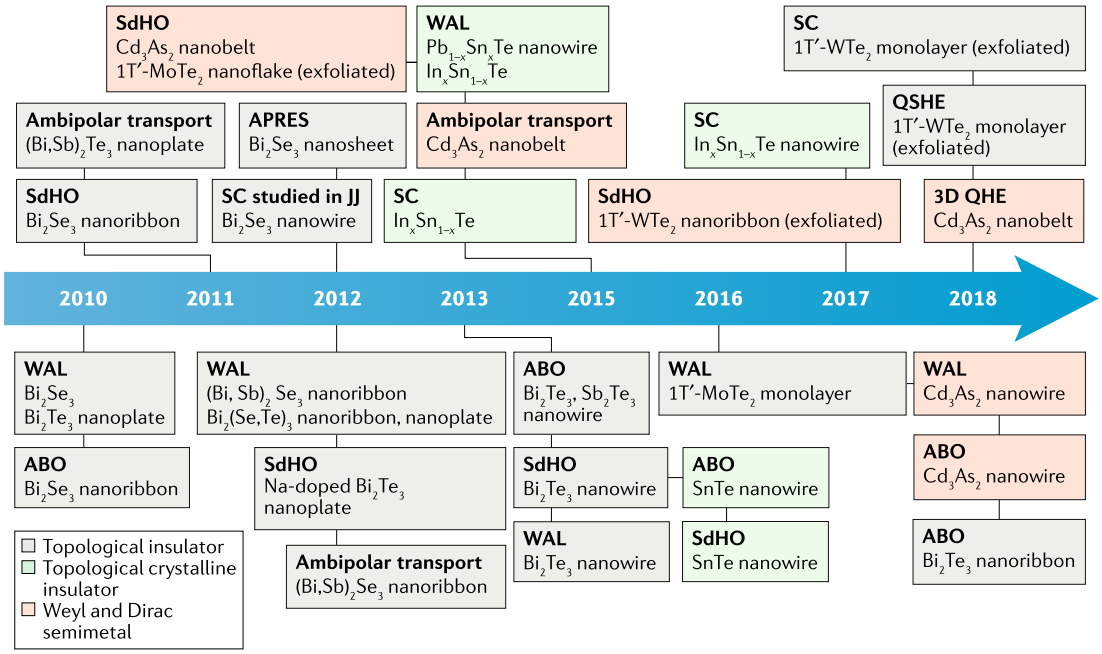

Fig. 3 | **Historical timeline of transport measurements in topological nanostructures.** Transport results probing the nature of the surface states in topological nanostructures. Before the discovery of topological insulators, many topological materials were extensively studied for thermoelectric properties, but those results are omitted for brevity. ABO, Aharonov–Bohm oscillation; ARPES, angle-resolved photoemission spectroscopy; JJ, Josephson junction; QSHE, quantum spin Hall effect; SC, superconductivity; SdHO, Shubnikov–de Haas oscillation; WAL, weak antilocalization.

rhombohedral structure[125,126]. This structural phase change is associated with a ferroelectric transition and mediated by electron–phonon interactions[127]. Theoretically, Dirac cones on {001} surfaces are predicted to become gapped owing to the loss of crystal symmetry, whereas the ones on {111} surfaces are expected to remain intact. The structural transition has been observed in SnTe and $SnSe_xTe_{1-x}$ nanoplates[81,91], but its effects on the surface states have not been probed in transport measurements.

Indium-doped SnTe nanoplates and nanowires were reported to show superconductivity. The In-doped SnTe nanoplates were synthesized on silicon substrates from SnTe and InTe powders as precursors and a gold film as metal catalyst for growth[89]. The In doping concentration varied from 0% to 10% with a loading ratio of SnTe:InTe = 1:2. Transport data showed the onset of superconductivity around 1.7 K (FIG. 5a). The bulk crystal growth, chemical vapour transport, was also adapted by inserting silicon substrates inside the sealed quartz tube to grow In-doped SnTe nanoplates without the use of metal catalysts or transport agents[90] (FIG. 5b). An In-doped SnTe bulk crystal was first grown by mixing high-purity elements and then used as source for the nanoplate growth. A sharp transition to the superconducting regime was observed with a critical temperature just below 2 K, similar to the result shown in FIG. 5a.

A desired nanostructure for quantum computations is superconducting SnTe in nanowire form, which was first synthesized in 2017. In-doped SnTe nanowires were obtained using gold nanoparticles as growth catalysts, and SnTe and InTe as source and dopant powders, respectively[128]. In the same growth, nanoplates, nanoribbons and nanowires were obtained, with their classification loosely determined by the width of the nanostructures. All of the nanostructures became superconducting below 2 K but displayed important differences (FIG. 5c). Nanoplates exhibited a sharp transition into a superconducting regime but, interestingly, the resistance began to increase from zero to finite values at temperatures below 400 mK. Nanoribbons showed a gradual transition into the superconducting regime. Nanowires showed non-zero residual resistance after transitioning into the superconducting regime. The origin of this non-zero resistance is unclear. Quantum effects such as quantum phase slips due to nanoscale confinement and potential contact issues have been ruled out. A mundane reason could be material issues, such as inhomogeneous distribution of In dopants or the presence of Au atoms as impurities. Au atom impurities have been observed in some Au-catalysed SnTe nanostructure growth[129]. However, such material imperfections should also be present in nanoplates. The non-zero resistance in superconducting In-doped SnTe nanowires needs to be further investigated.

Weyl and Dirac semimetal nanostructures. The study of the predicted surface Fermi arcs through transport measurements in Weyl and Dirac semimetals is challenging, because the bulk metallic states are always present in these materials, making up a large fraction of the transport signal. Nanostructures can be advantageous because of their high surface-to-volume ratios, which can minimize the contribution from the bulk states. Moreover, by controlling the morphology of the nanostructures to maximize specific crystallographic planes,

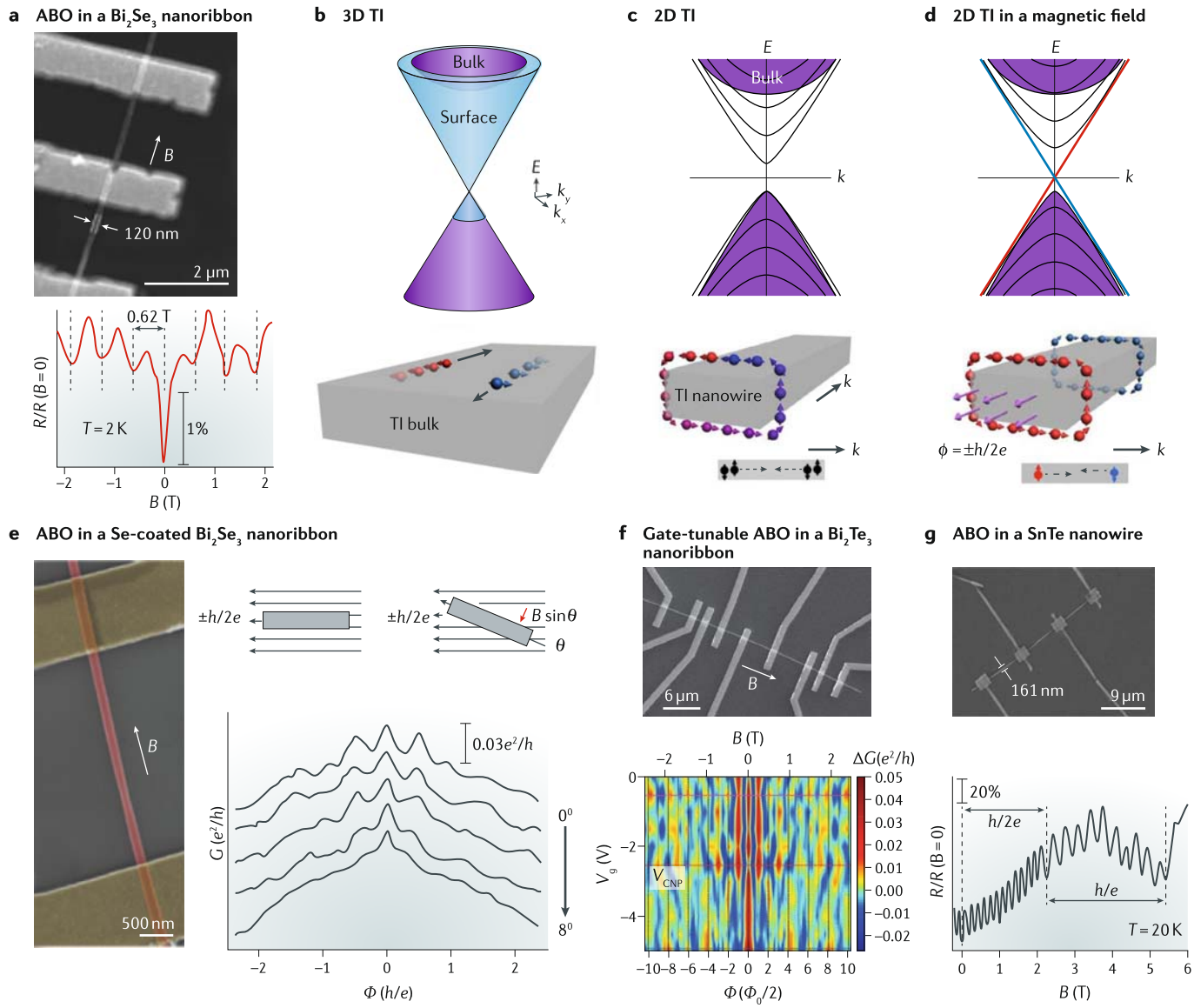

Fig. 4 | **Aharonov–Bohm effects of topological surface states in TI and TCI nanostructures. a** | Scanning electron microscope (SEM) image of a 120-nm-wide, 55-nm-thick Bi_2Se_3 nanoribbon contacted by four Ti/Au electrodes. In this system, magnetoresistance (R) oscillations with a period of 0.62 T, corresponding to one flux quantum (h/e) threaded into the cross-section of the nanoribbon, are observed at 2 K. **b** | Schematic band structure of the 3D topological insulator (TI) Bi_2Se_3. The surface states (blue) exist inside the gap of bulk bands (purple). Topological surface electrons are spin-polarized (red and blue arrows). **c** | Schematic band structure of a TI nanowire in zero magnetic field. The surface band transforms into discrete 1D sub-bands with spin degeneracy. The 2π rotation of the helical surface electron spin along the nanowire perimeter gives rise to a Berry's phase (π) in the electron wavefunction, which opens a gap in the 1D bands. **d** | Schematic band structure of a TI nanowire with magnetic flux $\Phi = \pm h/2e$ (purple arrows). The gapless 1D band (red and blue lines) is predicted to be a topologically non-trivial electronic state with no spin degeneracy. Electrons with opposite spin orientations propagate in opposite directions. **e** | SEM image of a Bi_2Se_3 nanoribbon device. Adding a perpendicular magnetic field component by rotating the device breaks the time-reversal symmetry condition at $\Phi = \pm h/2e$, resulting in localized helical 1D modes in a disordered TI nanowire. Quantum interference (helical 1D peaks at $\Phi = \pm h/2e$) is suppressed as the angle θ increases, as seen in the conductance (G) plots. **f** | SEM image of a 150-nm-wide, 60-nm-thick Bi_2Te_3 nanoribbon device. The colour map of the magnetoconductance ΔG versus gate voltage V_g and magnetic field B shows Aharonov–Bohm oscillations (ABO) with $\Delta G(B)$ maxima at both odd multiples of $\Phi_0/2$ (half-integer flux quanta, unique to topological surface states) and even multiples of $\Phi_0/2$ (except at $\Phi = 0$), suggesting a competition between π-ABO and 0-ABO at different V_g. **g** | SEM image of a 161-nm-wide, 240-nm-thick SnTe nanowire device. The magnetoresistance curve displays two oscillation frequencies, h/e (0.313 T) and $h/2e$ (0.165 T), indicating the diffusive transport regime. Panel **a** is adapted from REF.[56], Springer Nature Limited. Panels **b**–**e** are adapted with permission from REF.[57], ACS. Panel **f** is reproduced from REF.[59], Springer Nature Limited. Panel **g** is adapted with permission from REF.[60], ACS.

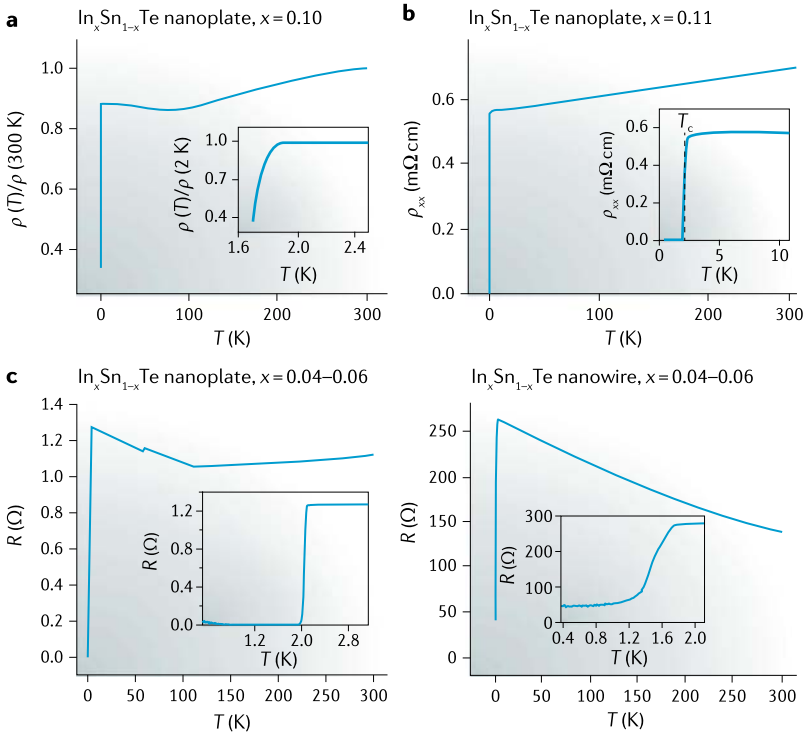

Fig. 5 | **Superconducting transitions in various $In_xSn_{1-x}Te$ nanostructures.** **a** | Temperature dependence of the normalized resistivity ρ of a nanoplate device with $x = 0.10$ and a thickness of 346 nm, showing a superconducting transition at 1.7 K. **b** | Temperature dependence of the resistivity of a nanoplate device with $x = 0.11$ and a thickness of 57 nm, showing a superconducting transition at 2.2 K. **c** | For a nanoplate device with $x = 0.04$–0.06, the superconducting transition occurs below 2.1 K. An upturn in the resistance R below 0.4 K is also observed. For a nanowire device with $x = 0.04$–0.06 and a width of 193 nm, the superconducting transition is gradual, and the resistance saturates to $R \approx 55\ \Omega$ at the base temperature. Panel **a** is adapted with permission from REF.[89], ACS. Panel **b** is adapted with permission from REF.[90], ACS. Panel **c** is adapted from REF.[128], CC-BY-4.0.

it may be possible to perform momentum-selective transport measurements. This is important because the surface Fermi arcs start and end at well-defined points in momentum space.

Owing to the challenges related to the synthesis of these materials, most electron transport studies of Weyl and Dirac semimetals have used bulk crystals, but some transport studies on nanostructures are available, and here we discuss a few. Cd_3As_2, a type I Dirac semimetal, was synthesized as nanowires, and ambipolar transport was achieved by field-effect tuning of the Cd_3As_2 nanowire device[61]. A Hall-bar device based on a Cd_3As_2 nanobelt showed anomalous, double-period Shubnikov–de Haas oscillations that resulted from two ellipsoidal Fermi surfaces, suggesting the dimensionality-dependent transport expected of a 3D Dirac semimetal[61]. Aharonov–Bohm oscillations were also observed in a Cd_3As_2 nanowire device with the peak positions at odd integers of $\Phi_0/2$ with a period of Φ_0, suggesting the presence of topological surface states[108]. Negative magnetoresistance was also observed in the nanowire and attributed to the chiral anomaly, a phenomenon that involves a current flow between the Weyl nodes in the presence of parallel electric and magnetic fields[130]. A negative magnetoresistance is expected in a Dirac semimetal owing to its topological nature, but mundane effects, such as disorder in the system, can also lead to negative magnetoresistance. Thus, systematic transport studies that rule out other effects are critical. Recently, Weyl orbits in a Cd_3As_2 nanobelt were reported to contribute to the 3D quantum Hall effect: transport measurements highlighted a dependence of the Landau levels on the sample thickness, unveiling the 3D signature of this new type of quantum Hall effect[131] (FIG. 6a). This is the first time the quantum Hall effect is observed in an intrinsically 3D crystal. Previously, wedge-shaped Cd_3As_2 slabs were prepared by milling of the bulk crystal by a focused ion beam[132]. The benefit of using nanostructures directly rather than focused ion beam milling is that no material damage is induced during the preparation, enabling the investigation of morphology-dependent transport to study the Weyl or Dirac state.

Some transition metal dichalcogenides are predicted to be Weyl semimetals, such as 1T′-$MoTe_2$ and 1T′-WTe_2. Chiral-anomaly-induced negative magnetoresistance and Fermi-arc-induced Weyl orbit oscillations were observed in an exfoliated 1T′-WTe_2 nanoribbon, providing evidence that WTe_2 is a type II Weyl semimetal[110] (FIG. 6b). A bandgap opening of ~60 meV was also observed by absorption spectroscopy in exfoliated 1T′-$MoTe_2$ flakes[109]. Recently, superconductivity induced by field-effect gating was observed in monolayer WTe_2 (REFS[133,134]), which is exciting, as monolayer WTe_2 was established as a 2D TI with a quantum spin Hall state that persisted up to 100 K (REF.[135]), a temperature easily accessible with liquid nitrogen for practical device realization. The quantum spin Hall state and the superconducting transition were realized in the same device by tuning the top and bottom gate voltages below 1 K, offering a promising route to explore a 2D topological superconductor (FIG. 6c). All transport measurements were carried out on exfoliated samples that were encapsulated with hexagonal boron nitride, which provides an inert electric environment and prevents oxidation.

Inducing superconductivity in topological nanostructures. Topological quantum computation might be made possible by inducing superconductivity in topological nanowires to produce MBSs. Two routes to induce superconductivity into topological materials have been attempted. The first option is to place topological materials next to a superconductor to induce superconductivity by proximity. This was tried in Bi_2Se_3, Bi_2Te_3 and Sb-doped Bi_2Se_3 flakes exfoliated from bulk crystals or synthesized as nanoribbons and films, which were proximitized with superconducting metals and showed unconventional properties when characterized with Josephson junction devices[104,106,107]. Another route to induce superconducting correlations in topological materials is by intercalation or doping. In bulk crystals, superconductivity has been demonstrated in metal-intercalated TIs, such as Cu-intercalated, Sr-intercalated and Tl-intercalated Bi_2Se_3 and Bi_2Te_3 (REFS[136–138]) and Sb_2Te_3 of a specific stoichiometry[139], In-doped SnTe (REFS[140–142]), and WTe_2 and $MoTe_2$ under pressure or

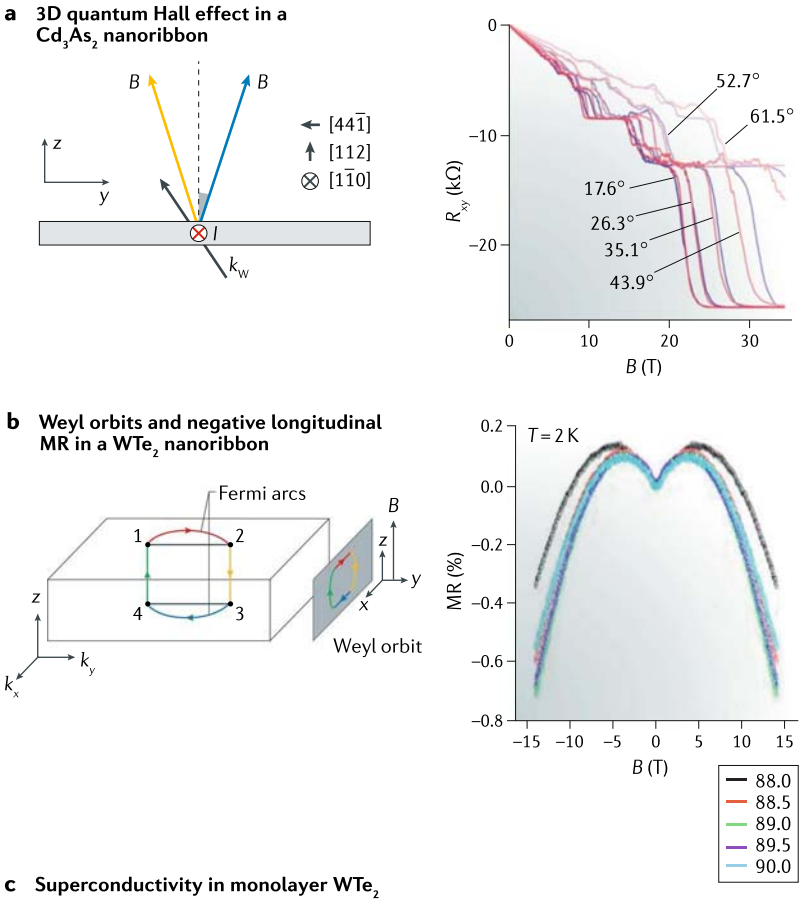

Fig. 6 | **Electron transport studies of Weyl and Dirac semimetals. a** | Angular dependence of the 3D quantum Hall effect in a Cd_3As_2 nanoribbon. The schematic shows the measurement geometry. The grey arrow denotes the Weyl vector k_W, which is defined by a pair of Weyl nodes along the [100] axis. The magnetic field B is tilted by a positive or negative angle θ, marked by the blue or yellow arrow. In the Hall resistance (R_{xy}) plot, notable deviations can be observed between R_{xy} measured at positive and negative tilt angles (red and blue curves, respectively), which are attributed to the existence of Weyl nodes and to the Zeeman effect. Such deviations are not expected to occur owing to thickness-modulated changes in the Fermi level or band structure. **b** | Fermi-arc-induced Weyl orbits and chiral-anomaly-induced negative longitudinal magnetoresistance (MR) in a WTe_2 nanoribbon. The formation of the Weyl orbit under a magnetic field in a WTe_2 nanoribbon is illustrated in the left part. Two pairs of Weyl nodes (1–2 and 3–4) with opposite chirality are connected by two real-space paths through chiral bulk Landau levels along the z direction and by two Fermi arcs in momentum space. The field-angle dependence of the negative longitudinal magnetoresistance shows that the absolute value of the magnetoresistance decreases significantly with a minor change of the field angle θ from 90° to 88°, which is a signature of magnetoresistance induced by the chiral anomaly. **c** | Superconductivity was observed in a gated monolayer WTe_2 device, shown in the top part. The voltage–current (V–I_{dc}) and dV/dI versus I_{dc} behaviours of this device at various temperatures and magnetic fields are shown. A zero-voltage plateau is observed at 60 mK, confirming the superconducting state in the WTe_2 single-layer sheet. Panel **a** is reproduced from REF.[131], Springer Nature Limited. Panel **b** is adapted from REF.[110], CC-BY-4.0. Panel **c** is adapted with permission from REF.[133], AAAS.

doping[143–146]. The nature of the superconductivity and the question of whether it is topological need further study; evidence for unconventional superconductivity has been obtained in point-contact spectroscopic studies carried out on the surface of a Cu-intercalated Bi_2Se_3 bulk crystal and an In-doped SnTe bulk crystal[137,140,147].

Superconductivity has been demonstrated in a few topological nanostructures, including In-doped SnTe nanoplates and nanowires (TCI system)[89,90,128] and mechanically exfoliated monolayer WTe_2 flakes (TI system)[133,134]. Although metal intercalation into TI nanostructures has been demonstrated using various metal atoms, which induced changes in the electrical and optical properties[148,149], superconductivity has not been achieved in metal-intercalated TI nanostructures.

1D topological superconductivity

Currently, there is an intense focus on realizing and manipulating MBSs for topological quantum computations. Topological nanowires are uniquely suitable for this purpose. In this section, we discuss 1D topological superconductivity and how to control the expected MBSs in such systems.

Before the discovery of TIs, topological phases of superconductors were predicted to exist for p-wave pairing of 2D fermions[150–152]. When TIs were discovered, a direct analogy between TIs and superconductors was observed: the Bogoliubov–de Gennes equation for

a *p*-wave superconductor is identical in structure to the Dirac equation, although the two equations have different origins. As TIs exhibit novel excitations at the intersection of gaps of different sign, for example, at the surface of the TI material, so do topological superconductors, producing MBSs at zero energy on the surface of a topological superconductor. Topological nanowires offer unique control over the topological superconducting states, providing clear advantages over other materials that may host MBSs.

The basics of 1D topological superconductivity and of the creation of MBSs in 1D systems are explained in BOX 2, which describes a helical metal that mimics the spinless Kitaev model. A topological superconducting state can be induced in the helical state by adding superconducting correlations.

Spin–orbit coupled nanowires versus TI nanowires. Two classes of nanowires have been studied to search for MBSs: nanowires made from topological materials, such as TI Bi_2Se_3 (REF.[104]) or TCI SnTe (REF.[153]), and nanowires made from semiconductors with strong spin–orbit interactions, such as InAs or InSb (REFS[64,105]). For the TI case, we will only consider systems with a single Dirac cone, such as Bi_2Se_3. In systems in which multiple Dirac cones are present, as in TCIs, it is also possible to host MBSs[21,82], and the control mechanics described here are equally applicable. Adding superconducting correlations into TI nanowires or semiconducting nanowires with spin–orbit interactions is typically done by doping, as in the case of In-doped SnTe, or by exploiting the proximity effect, in which a superconductor is placed in contact with the material, and superconducting correlations are allowed to 'leak' in.

The most experimentally explored topological superconducting systems thus far are 1D semiconducting nanowires with strong spin–orbit coupling, such as InAs and InSb nanowires grown by molecular beam epitaxy[64] or metal-organic CVD[105]. The focus on these systems is largely because the crystal quality of these nanowires is currently much better than that of other material systems, including TI nanowires. The energy band structure for semiconducting nanowires is shown in FIG. 7a: the conventional parabolic dispersion is split along the

Box 2 | **Kitaev model for a spinless 1D wire with *p*-wave superconducting pairings**

The canonical model that captures the physics of topological superconductivity was originally developed by Kitaev[150]. Kitaev considered a 1D wire of spinless fermions with *p*-wave superconducting pairing and *N* total sites. The Hamiltonian is

$$H = -\mu\sum_j c_j^\dagger c_j - \frac{1}{2}\sum_j\left(-\omega\left(c_j^\dagger c_{j+1} + c_{j+1}^\dagger c_j\right) + \Delta c_j c_{j+1} + \Delta^* c_{j+1}^\dagger c_j^\dagger\right) \quad (2)$$

where c_j and $c_j^\dagger$ are creation and annihilation operators at site *j*, respectively, ω is the nearest-neighbour hopping strength between sites (labelled *j*), μ is the chemical potential and $\Delta = |\Delta|e^{i\phi}$ is the *p*-wave pairing amplitude. We can rewrite this Hamiltonian by defining the creation and annihilation operators in terms of two Majorana bound states (MBSs; $\gamma_{A,j}$ and $\gamma_{B,j}$) at each site *j*, and combine the superconducting pairing phase ϕ to get $c_j = \frac{1}{2}e^{i\phi}(\gamma_{A,j} + \gamma_{B,j})$. The Hamiltonian becomes

$$H = -\frac{\mu}{2}\sum_j^N\left(1 + \gamma_{A,j}\gamma_{B,j}\right) - \frac{i}{4}\sum_j^{N-1}\left[(\omega + |\Delta|)\gamma_{A,j+1}\gamma_{B,j} + (-\omega + |\Delta|)\gamma_{A,j}\gamma_{B,j+1}\right] \quad (3)$$

We can consider two limiting cases. When $\mu \neq 0$ (and $\omega = \Delta = 0$), each pair of MBSs is paired on a site *j* (panel **a** of the figure). However, when $\mu = 0$ and $\omega = |\Delta|$, the Hamiltonian is given by $H = i\omega\sum_j^{N-1}\gamma_{A,j+1}\gamma_{B,j}$. In this scenario, an MBS on site *j* is coupled to an MBS on $j+1$ or $j-1$ and, importantly, the MBS A at $j = 0$ and the MBS B at $j = N$ are not coupled to their neighbour and do not appear in the Hamiltonian: the system supports unpaired zero-energy MBSs at the end of the chain (panel **b** of the figure). In the Kitaev model, the fermionic operators are written in terms of two MBSs, which can be done for any system. This is just a mathematical construct, as the two MBSs are localized at the same spot. The key is that under the right conditions ($\mu = 0$ and $\omega = |\Delta|$), the system undergoes a phase transition accompanied by the opening of a topological gap[150], resulting in a pair of MBSs being localized far apart. Pairs of non-local MBSs like those at the ends of a 1D chain form a highly degenerate ground state, and exchange of any two such MBSs transforms the state in a non-commutative way, exhibiting non-Abelian statistics[152]. In this toy model, MBSs do not exist only at $\mu = 0$ and $\omega = |\Delta|$. An investigation of the parameter space shows regions with topologically trivial and non-trivial gaps (panel **c** of the figure)[190], which can be tuned by changing μ with a gate voltage. At $\mu = |\omega|$, a topological quantum phase transition occurs, and as long as μ is within the absolute value of ω, the phase is topological.

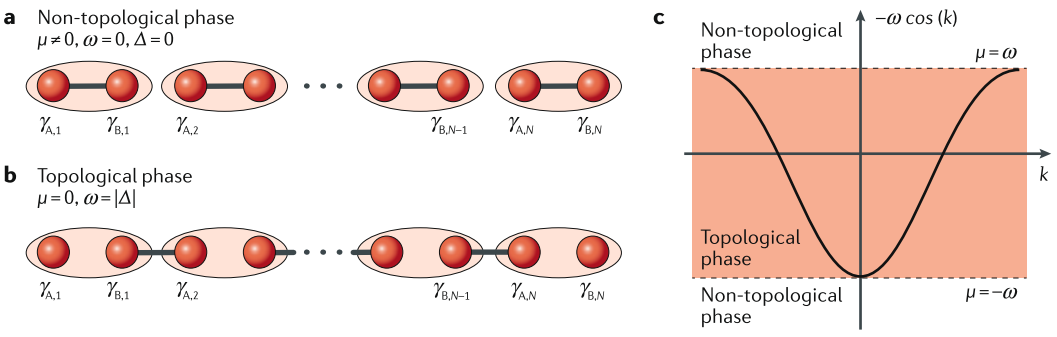

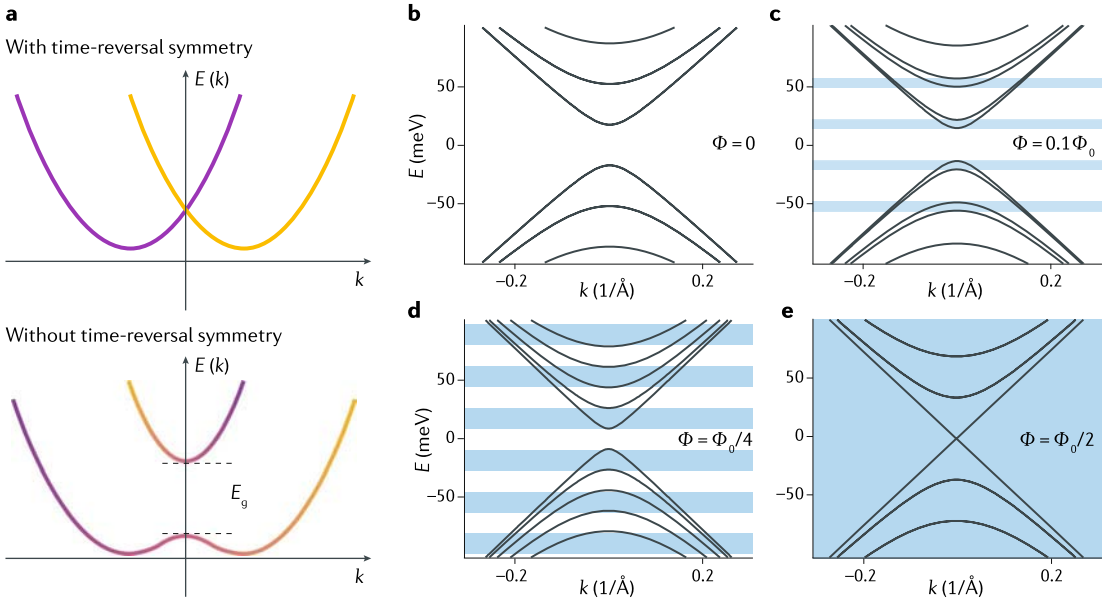

Fig. 7 | **1D topological superconductors. a** | Band structure for a material with strong spin–orbit coupling in the presence and absence of time-reversal symmetry. To achieve a helical state, the Fermi energy must be in the energy gap E_g. The yellow and purple colours indicate spin orientation up and down, respectively. **b–e** | Band structure for a nanowire of a strong topological insulator material with a radius of 100 nm as a function of magnetic flux, Φ; Φ_0 is the quantum of flux. For certain values of the chemical potential (shown in blue), the wire meets the criterion for topological superconductivity. When $\Phi = \Phi_0/2$, the wire is in the helical phase for all values of the chemical potential.

k-axis from the spin–orbit interaction. When time-reversal symmetry is present, the Kramers degeneracy at $k = 0$ must be preserved, and there is a twofold spin degeneracy ($E_\uparrow(k) = E_\downarrow(-k)$). This degeneracy can be broken by removing the time-reversal symmetry, which is most commonly achieved by applying a magnetic field perpendicular to the spin–orbit field. When this is done, the Kramers degeneracy at $k = 0$ is removed, and one of the double-degeneracies at the Fermi energy is absent. It is in this sense that the 1D wire is spinless and has the potential to realize Kitaev's model. Under these conditions, the wire is said to be helical when the Fermi energy is within the gap that forms, which has energy E_g. The term helical refers to the fact that the spin eigenvalue is associated with the direction of propagation. The progress on synthesis and transport results on spin–orbit coupled semiconducting nanowires is summarized in a recent review[64].

In strong TI nanowires, a helical surface state can also be obtained but, unlike in strong spin–orbit coupled nanowires, time-reversal symmetry is preserved. The energy spectrum of eigenstates in a strong TI nanowire is given by

$$\varepsilon_{n\pm} = \pm\hbar v_s \sqrt{\left[\left(n + \frac{1}{2} - \frac{\Phi}{\Phi_0}\right)/R\right]^2 + k^2} \qquad (1)$$

Here, $\hbar$ is the reduced Planck's constant, v_s is the surface velocity of electrons, k is the momentum along the wire, $n = 0, \pm1, \ldots$ are the angular momentum states around the wire, Φ is the magnetic flux through the wire, R is the radius of the wire and Φ_0 is the quantum of flux. What is important is that a zero-energy mode is created when a half flux quantum, $\Phi_0/2$, is passed through the wire. Given the flux-dependent band structure, the criterion for the TI wire to host MBSs when superconducting correlations are introduced can be analysed by looking at the degeneracy of each level as a function of the magnetic field. When $\Phi = 0$, each level is doubly degenerate from different angular momentum states with the same energy (for example, $\varepsilon_{0-} = \varepsilon_{-1+}$ at $\Phi = 0$) and each MBS is doubly occupied (that is, it forms a conventional fermionic mode; FIG. 7b). The application of small parallel magnetic fields allows for these level degeneracies to be broken, so that regions of energy levels with odd occupancy grow with magnetic field (blue regions in FIG. 7c,d); in these regions, the criterion for topological superconductors containing MBSs is met. For $\Phi = \Phi_0/2$, and for a range of neighbouring values[154], only odd occupancies are permitted, and a state with MBSs is permitted for all values of the Fermi energy (FIG. 7e). Thus, topological superconductivity can be controlled both with a magnetic field and, when $\Phi \neq 0$ or $\Phi_0/2$, with a gate voltage. Typically, chemical potential changes of 200 meV can be obtained using a field-effect geometry, and it is possible to tune the chemical potential entirely through the zero-energy Dirac point[72].

Also of importance is the preservation of time-reversal symmetry when $\Phi = \Phi_0/2$. At $\Phi = 0$, each level is twofold degenerate (FIG. 7b). The application of $\Phi_0/2$ along the axis of the wire produces an Aharonov–Bohm phase difference of $\theta_{AB} = \int A \cdot dl = 2\pi$ between time-reversal symmetry paths, where dl is a vector of unit length along the circumference of the wire, and this trivial phase preserves the twofold degeneracy observed when time-reversal symmetry is present. It is important to note that, unlike in conventional materials,

the zero-field Kramers pairs are not the same pairs at $\Phi = \Phi_0/2$. For example, ε_{0-} and ε_{-1+} are degenerate at $\Phi = 0$, but ε_{0-} and ε_{0+} are degenerate at $\Phi = \Phi_0/2$. The swap of Kramers pairs is a hallmark of the Z_2 classification of the topological state obtained at $\Phi = \Phi_0/2$ (REF.[155]).

The key transport property of TI nanowires that indicates the presence of the topological surface state is the presence of Aharonov–Bohm oscillations. However, a mere observation of the Aharonov–Bohm effect is not sufficient to probe the topological nature of the surface state. Conduction maxima at odd values of $n\Phi_0/2$ also have to be observed[156]. This is to be contrasted with a conventional Aharonov–Bohm effect where maxima are predicted at even values of $n\Phi_0$, including $n = 0$. Experimental work has shown that TI nanowires do in fact conform to the theoretical expectation, as shown in FIG. 4f for a Bi_2Te_3 nanowire[59]. When the Fermi level is placed at or near the charge neutrality point, peak conduction values occur at odd integers of $\Phi_0/2$. This persists for a small range of gate voltages on the hole side of the charge neutrality point before a conventional Aharonov–Bohm phase is observed, purportedly arising when the Fermi level enters the bulk valence band.

Generating a helical state in this way in TI nanowires offers several advantages over strong spin–orbit coupled nanowires. The first is that no fine tuning of the energy level is required. For strong spin–orbit coupled nanowires, the location of the Fermi energy plays an important role in creating MBSs rather than trivial zero-energy Andreev bound states[157]. Unlike strong spin–orbit coupled nanowires in which the helical state exists only over a narrow range of energies, at $\Phi = \Phi_0/2$ strong TI nanowires are guaranteed to be in the topological state regardless of the location of the Fermi energy, provided the Fermi energy lies in the bandgap. This also alleviates the role of additional subbands, which have been experimentally shown to mask the interpretation of evidence for the helical state[158]. The second advantage is that for strong TI nanowires coupled to conventional *s*-wave superconductors, the $p + ip$ superconducting state can be created when time-reversal symmetry is preserved, and the resulting superconductivity is immune to disorder, as it is protected by Anderson's theorem[159]. The helical nature of the surface state in the TI guarantees that the induced superconductivity is $p + ip$ in nature, which allows for much larger energy scales for the MBSs, enhancing the prospects for creating this unique superconducting state[159]. The third advantage is that a magnetic field can be used to create and control the topological superconducting state. This should be contrasted with the use of electric fields in spin–orbit coupled nanowires, which can be complicated by the fact that the MBSs exist very near a superconductor whose high density of electrons can obfuscate applied local electric fields for the control of the MBSs.

Prospect for 1D topological superconductors using TI nanowires. The control over the formation and location of MBSs is of utmost importance in the progression towards the use of MBSs in a topological quantum computer: for braiding operations to be performed, MBSs must be manipulated locally. Gate control of the location of an MBS is possible with an electric field, although it is difficult owing to the proximity of the superconductor, which screens the electric field in the wire. Here, we investigate the possibility of controlling the location of an MBS with magnetic fields by using local *B* control gates made of current-carrying wires (FIG. 8). For TI nanowires with diameters as large as 300 nm, the parallel magnetic fields needed to create the topological superconducting state are as small as 23 mT. Current-carrying wires near the TI wire can locally produce magnetic fields that are an appreciable fraction of 23 mT. As a proof of principle, we present a finite element method simulation of three nearby wires (cross-section of 300 nm by 300 nm; the superconductor is not included in the simulations). Current is passed through one or all three of the wires (*B* control gates; FIG. 8) to generate a component of magnetic field B_x along the axis of the wire. In this configuration, the topological quantum phase transition is tuned by two sources: a global magnetic field supplied by a large superconducting solenoid and a local magnetic field supplied by the *B* control gates. The spatial distribution of the *x* component of the magnetic field generated by passing 1 mA of current through the central wire is shown in FIG. 8a, in which the dotted contour indicates $B_x = 5$ mT. If the global field is set to 5 mT below the value corresponding to the phase transition, two MBSs (the red circles) arise where the 5 mT contour line intersects the nanowire. As an example, the magnetic field necessary for the phase transition for a 100-nm nanowire is 212 mT, so in this scenario the solenoid would be set to 207 mT, and the local gate would provide the extra 5 mT to drive the transition. Here, unlike in the case of electric-field gating in which the superconductor hinders the Fermi energy control, the screening (Meissner) properties of the superconductor enhance the parallel magnetic field seen by the wire, and 5 mT represents a lower bound on the magnitude of the field. If the current in the outer two wires is increased to 1/3 mA, the MBSs are pushed towards the ends of the nanowire (FIG. 8b) and finally to the ends of the nanowire when all the *B* control gates have currents of 1 mA (FIG. 8c). This technique can be used to test fusion rules and, in T-shaped nanowires, to perform braiding operations and readout as prescribed in REF.[63]. MBS detection through thermal transport (FIG. 8d) is discussed in a later section.

Key challenges

For the realization of topological quantum computers that are resistant to errors, synthesizing robust 1D topological superconductors using topological nanowires is critical. However, several challenges remain. Efforts into studying superconducting topological nanowires should be accompanied by active research in various topological nanomaterials and nanostructures to tackle the synthesis and transport challenges specific to nanoscale systems.

Material challenges. Controlling the crystal quality and morphology of topological nanostructures remains difficult. For example, for chalcogen-based TIs and TCIs such as Bi_2Se_3, Bi_2Te_3 and SnTe nanostructures, defect densities, primarily chalcogen vacancies, remain high, contributing to a high residual bulk carrier density.

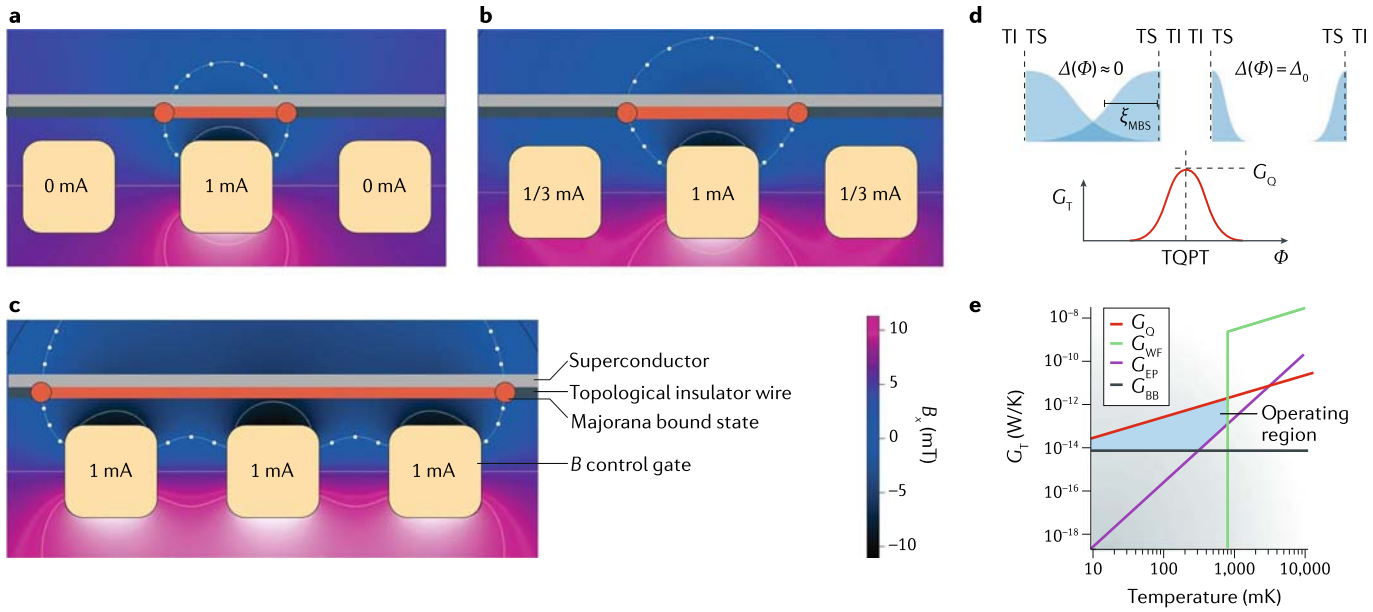

Fig. 8 | **Controlling and detecting Majorana bound states in topological insulator nanowires. a–c** | Finite element simulations for the magnetic field (B) profile generated by three B control gates, each 300 × 300 nm, used to manipulate the position of a pair of Majorana bound states (MBSs, red circles). The values of the current in the three wires are indicated. The dotted contour indicates $B_x = 5$ mT. The central wire is used to drive the initial topological quantum phase transition that generates the pair of MBSs, and the outer two wires are used to drive the pair towards the end of the wire. **d** | MBSs in a topological insulator–topological superconductor–topological insulator (TI–TS–TI) device. Illustration of the spatial extent $\xi_{MBS} = hv_F/\Delta$ (where h is Planck's constant, v_F the Fermi velocity and Δ the size of the topological gap) of the MBSs in the wire near (left) and away from (right) the topological quantum phase transition (TQPT). The MBSs are shown only on the inside of the TI–TS interface, indicated by the dashed line. At the TQPT, the overlap of the two MBSs produces a peak in the thermal conductance G_T that is equal to the quantum of thermal conductance G_Q, regardless of the amount of disorder. **e** | Estimation of the contributions to G_T in a TI nanowire. Below $T \approx 800$ mK, G_Q is the largest of the four contributions (also considered: G_{WF}, thermal conductance from electrons described by the Wiedemann–Franz Llaw, presumed to be zero below the critical temperature of the superconductor; G_{EP}, thermal conductance from electron–phonon coupling, as calculated for Bi_2Se_3 (REF.[192]); G_{BB}, thermal conductance from blackbody radiation[193]), which leads to the definition of a proposed operating region (blue).

Vacancy defects persist, despite chalcogen-heavy synthesis conditions, owing to the low formation energies of vacancy sites. Thus, efforts to further reduce these vacancies or to find compensation doping schemes that do not degrade electron mobility are essential. Theoretical calculations of the energy levels of different dopants in topological materials would aid experiments. In addition, detailed knowledge on other types of defects, such as anti-site defects and line defects such as screw dislocations, is limited, even though these defects do doubtless degrade transport properties or induce new topological edge states. The recent surface characterization of CVD-grown SnTe nanostructures indicates a rather high density of screw dislocations embedded inside the nanostructures[160], most likely formed because of fast growth kinetics. Hence, more detailed characterizations of the microstructures of topological nanomaterials using aberration-corrected (scanning) transmission electron microscopy and spectroscopy techniques are critical. Transport properties of topological nanomaterials should then be correlated with defect densities and types, to find out the types of defects most important for transport properties. At present, such structure–property relation studies are almost non-existent for topological surface states. For example, the scattering mechanisms of the topological surface states as a function of impurities, crystal defects or surface oxidation are all important, yet largely unknown. Detailed studies of structure–transport property relations were key in developing many of today's high-end electronic and optoelectronic technologies. The same intense efforts must be made for topological nanomaterials.

To fully realize the potential of topological nanostructures and 1D topological superconductors, serious efforts must be dedicated to the synthesis of topological nanostructures, accompanied by detailed structural, chemical and transport characterizations. Property metrics for the crystal quality should be defined; these are often tied to specific technological applications or scientific objectives. The two most useful metrics would be the placing of the Fermi level within the bulk bandgap, and carrier mobilities of at least ~2,000 $cm^2 V^{-1} s^{-1}$ for TI and TCI nanostructures. Samples exhibiting these properties will enable routine observation of quantum effects from the topological surface states in temperature and magnetic field ranges that are easily accessible in laboratories. To achieve these property metrics, which require improved material quality and controlled nanostructure morphology, understanding the growth mechanism of topological nanomaterials becomes essential. Because

topological nanomaterials are often made by VLS or CVD growth methods at high pressures in the presence of volatile gaseous precursors, understanding nucleation and growth is difficult. The lack of in situ diagnostic tools during growth contributes to challenges associated with nanostructure growth. Some laudable efforts have been made by using in situ TEM growth studies of semiconducting nanowires catalysed with gold nanoparticles to try to understand VLS growth. Detailed analysis of these experiments has shown the complexity of the growth process[161–164], the control of which requires precise knowledge of chemical potentials of various reaction gases, local growth temperature, growth pressure and the flow dynamics of reaction gases. For VLS growth, detailed understanding of the energy balance at the triple junction, the point at which the liquid metal catalyst, reaction gases and solid nanowire meet, is critical[164]. For CVD growth, its wide application to the growth of 2D transition metal dichalcogenides has led to notable efforts in studying the growth dynamics, which incorporates flow dynamics of carrier gases and source vapours at the macroscopic scale with bonding interactions at the site of nucleation and growth at the molecular level[165–168]. The role of growth substrates and of different types of precursors and additives should also be considered carefully for CVD. The systematic growth study of TCI SnTe and its alloys as nanostructures on various substrates has shown the huge effect that the substrate or the local chemical potential of precursors can have on the morphology of the final nanostructures[84,85].

An additional challenge, particularly for nanowire synthesis, is the control of the nanowire diameter. In growing Bi_2Se_3 nanoribbons using a gold catalyst, side growth from direct vapour-to-solid deposition occurs easily, widening the nanoribbon. This is undesirable for realizing 1D topological superconductors. Controlling doping is also problematic: for SnTe nanowires, the yield of In-doped SnTe nanowires with a dopant concentration high enough to induce superconductivity around 2 K remains low. Because the morphology of the nanostructures is governed by the minimization of the overall surface energy via the Wulff construction, careful investigation of the surface energies of different crystallographic facets with different atomic plane termination is important to predict and control the nanostructure morphology. The variation of the surface energies with local chemical potentials of various source vapours will also need to be taken into consideration. Some detailed studies have been carried out for SnTe nanostructures; for example, the surface energies of different crystallographic planes were calculated as a function of the chemical potential of Sn or Te vapours[169,170]. Synthesis studies can be greatly aided by theoretical simulations.

Among topological nanowires, only SnTe nanowires have been demonstrated to superconduct by In doping. More topological nanowires should be made superconducting, so that the most suitable system for quantum computations can be found. Reproducing the induced superconductivity in metal-intercalated TI bulk crystals in narrow nanoribbons seems the next reasonable goal for the field. Recently, electrochemical intercalation of copper atoms into Bi_2Se_3 nanoribbons has been demonstrated[171]. This approach is promising to obtain doping within the narrow concentration window necessary for inducing superconductivity. At present, it is unclear whether it is intercalated copper atoms or substitutional copper atoms that donate electrons to Bi_2Se_3. Thus, the exact positions and role of copper atoms in Bi_2Se_3 should be studied, in particular in nanostructures. The observed superconductivity in monolayer WTe_2 is also promising[133,134]. The synthesis of $MoTe_2$ and WTe_2 as nanowires and the realization of a superconducting state into these nanowires would be an exciting achievement.

Another important thing to keep in mind is that surface passivation is essential to prevent surface oxidation and to preserve the transport properties of topological surface states. Finally, the search for new topological materials that may already possess more desirable transport properties must continue. Recent theoretical works that identified thousands of topological materials are exciting, but experimentally verifying and studying these proposed materials is daunting[172–174]. More theoretical guidance to narrow the list would be most welcome.

Challenges in detecting surface state properties. Unlike spectroscopic techniques — such as ARPES — that provide insight primarily on surface phenomena, electronic transport measurements comprise both surface and bulk contributions. Typically, transport is dominated by the large carrier concentration of the bulk, hiding the relatively minuscule contribution of the surface. This results in ambiguity in the interpretation of experimental data, as was evident in the investigation of weak antilocalization mentioned above, in which the number of surface Dirac cones was not clearly determined despite a clear recipe for its extraction. Hence, new types of probes are needed to probe the surface state in transport measurements unambiguously. Although no clearcut experimental method has yet been demonstrated, superconductor–TI–superconductor Josephson junctions provide a step in the right direction, showing that new detection methods can reveal more about the surface state than conventional transport measurements.

Josephson junctions have been used to enhance the contribution of the surface state relative to the bulk in TIs such as Bi_2Se_3 (REF.[104]), HgTe (REF.[175]), Pb-doped SnTe (REF.[153]) and Cd_3As_2 (REF.[176]). The origin of this enhancement lies in the mechanism by which Cooper pairs are transferred between the adjacent superconductors in the junction. This process is facilitated by the presence of two symmetric energy levels formed by the repeated process of Andreev reflection that happens at the interface between the superconductor and the weak link (FIG. 9a). These levels, called Andreev bound states, have a position relative to the Fermi energy that is dependent on the relative phase difference φ between the left and right superconductor forming the Josephson junction (FIG. 9b). The states depend sensitively on the transmission probability of an electron or hole in the weak link region, τ. As τ increases, the Andreev bound states vary more markedly as φ evolves from 0 to 2π, resulting in both a larger maximum supercurrent I_s and a more skewed current–phase relation[177] (FIG. 9c). Owing to spin–momentum locking, surface state carriers typically have a larger value

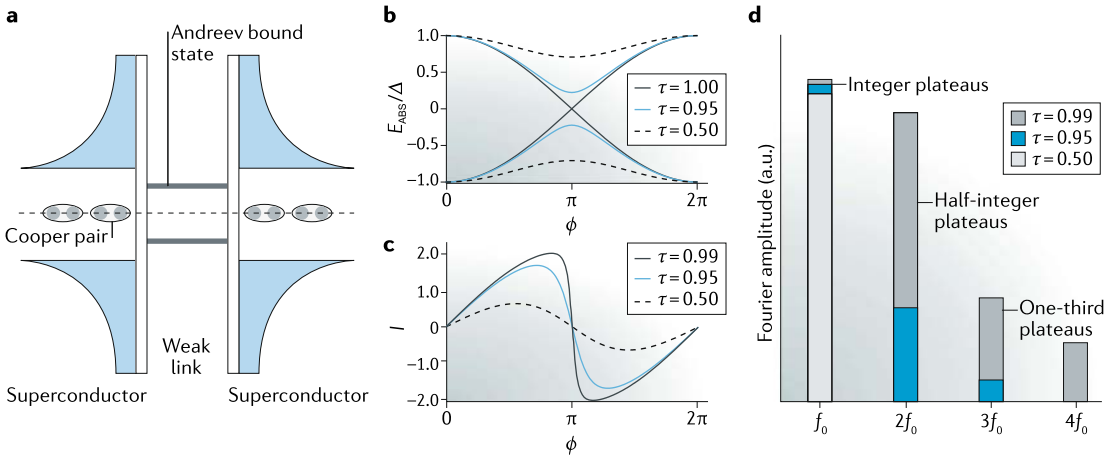

Fig. 9 | **Josephson junctions. a** | Schematic of a weak-link Josephson junction. A weak link made of conducting material facilitates transfer of Cooper pairs between two superconductors. **b** | Dependence of the Andreev bound states (ABSs) on the phase difference φ between the two superconductors for different values of the transmission probability τ, governed by the equation $E_{ABS} = \pm\Delta\sqrt{(1 - \tau \sin^2(\varphi/2))}$, where Δ is the size of the superconducting gap induced in the junction. **c** | Resulting current–phase relation for different values of τ. **d** | Varying harmonic content of the current–phase relation as a function of τ. Higher harmonic content results in the appearance of fractional (Shapiro) steps in the *I*–*V* (current–voltage) curve.

of τ than bulk carriers; hence, surface electrons have both a larger maximal supercurrent and skewness of the current–phase relation. This skewness has measurable effects on the properties of the junction. For example, the skewness of the current–phase relationship results in a curve with higher harmonic content as the value of τ approaches unity. This higher harmonic content modifies the properties of the current–voltage (I–V) curve under application of radiofrequency radiation, so that steps appear at quantized values (called Shapiro steps)[178]. The skewness of the current–phase relationship allows fractional step values to appear; a measurement of the Shapiro step size can uncover contributions from highly transmitting surface states, even in the presence of a large conducting background (FIG. 9d).

In addition to probing the surface state of TIs, the detection of MBSs in topological superconductors remains an important challenge in the investigation of superconducting TI and TCI nanowires. Although using charge transport to detect the helical mode is enticing, it suffers a drawback that plagues many of the charge transport experiments in superconducting TIs: unintentional doping of the bulk provides a large parallel conduction channel that can mask charges in electrical transport from the helical mode. This is reflected in FIG. 4f. The height of the conduction peak at $\Phi = \Phi_0/2$ is small, a fraction of e^2/h, whereas near the charge neutrality point a jump of e^2/h would be expected provided there is no contribution from the bulk. Furthermore, the role of the trivial bulk carriers in charge transport remains unclear. In systems with strong spin–orbit coupling, which include TI and TCI nanowires, additional geometric phases become important in understanding the overall phase acquired by electrons encircling the magnetic field. For example, in quantum rings fabricated from a 2D electron gas with strong spin–orbit coupling, a gate-dependent shift in the conductance maximum from even to odd values of $n\Phi_0/2$ has been observed[179]. The clear detection of the helical mode is essential to move forward with generating MBSs in superconducting TI and TCI nanowires.

Experiments with superconducting strong TIs have shown that supercurrents in Josephson junctions can be more sensitive to the helical nature of the surface states than charge transport experiments[175]. This phenomenon can be enhanced by the presence of a zero mode, whereby the sequential tunnelling provided by the zero-energy mode is much more efficient than the co-tunnelling process enabled by conventional Andreev bound states. Still, to pick out a contribution to the supercurrent of $e\Delta/h$ (which is 10 nA for aluminium leads) on top of a background that is 10^2 to 10^4 times larger can be difficult. A path forward might be provided by thermal transport: MBSs, being electrically neutral, naturally lend themselves to thermal transport. Theoretical work has demonstrated that a transition from a trivial ($\Phi = 0$) to a topological phase ($\Phi = \Phi_0/2$) is accompanied by a peak in the thermal conductance with a disorder-immune height of $G = G_Q$, the quantum of thermal conductance[180]. This technique has recently been used to explore the non-Abelian properties of the 5/2 quantum Hall state[181]. Although small, the thermal conductance arising from MBSs is expected to be dominant at low temperatures and within experimentally accessible values (FIG. 8d,e). Thermal transport may be the next breakthrough for work in topological superconductivity in strong TI nanowires.

Conclusions

Since the inception of band topology for condensed matter systems, the field of topological materials has grown greatly, with recent theoretical works suggesting that ~25% of all the materials we know may be topological in nature[182]. Studying them in nanostructures is important for potential device applications, such as topological field-effect transistors with fast-switching,

low-power topological magnetic memory devices and low-dissipation interconnects. The most attractive potential application for topological nanostructures is as qubits for robust quantum computers based on 1D topological superconductors; superconducting strong TI and TCI nanowires have been the most studied material candidates so far. Experimentally, much work is left, spanning from improving crystal quality and controlling the morphology of the topological nanostructures to developing transport measurement schemes that can overcome some of the limitations of charge-only transport measurements. Having witnessed the remarkable progress in the past decade in the field of topological materials, both theoretically and experimentally, it is exciting to imagine what lies ahead, particularly for topological nanomaterials.

Published online: 04 June 2019

1. König, M. et al. Quantum spin Hall insulator state in HgTe quantum wells. *Science* **318**, 766–770 (2007).
2. Kane, C. L. & Mele, E. J. Z_2 topological order and the quantum spin Hall effect. *Phys. Rev. Lett.* **95**, 146802 (2005).
3. Fu, L. & Kane, C. L. Time reversal polarization and a Z_2 adiabatic spin pump. *Phys. Rev. B* **74**, 195312 (2006).
4. Qi, X.-L. & Zhang, S.-C. Topological insulators and superconductors. *Rev. Mod. Phys.* **83**, 1057–1110 (2011).
5. Armitage, N., Mele, E. & Vishwanath, A. Weyl and Dirac semimetals in three-dimensional solids. *Rev. Mod. Phys.* **90**, 015001 (2018).
6. Dirac, P. A. M. The quantum theory of the electron. *Proc. R. Soc. A* **117**, 610–624 (1928).
7. Zhang, H. et al. Topological insulators in Bi_2Se_3, Bi_2Te_3 and Sb_2Te_3 with a single Dirac cone on the surface. *Nat. Phys.* **5**, 438–442 (2009).
8. Fu, L. & Kane, C. L. Superconducting proximity effect and Majorana fermions at the surface of a topological insulator. *Phys. Rev. Lett.* **100**, 096407 (2008).
9. Ren, Z., Taskin, A., Sasaki, S., Segawa, K. & Ando, Y. Large bulk resistivity and surface quantum oscillations in the topological insulator Bi_2Te_2Se. *Phys. Rev. B* **82**, 241306 (2010).
10. Kim, D. et al. Surface conduction of topological Dirac electrons in bulk insulating Bi_2Se_3. *Nat. Phys.* **8**, 459 (2012).
11. Xu, Y., Miotkowski, I. & Chen, Y. P. Quantum transport of two-species Dirac fermions in dual-gated three-dimensional topological insulators. *Nat. Commun.* **7**, 11434 (2016).
12. Zhang, Y. et al. Crossover of the three-dimensional topological insulator Bi_2Se_3 to the two-dimensional limit. *Nat. Phys.* **6**, 584–588 (2010).
13. Zhang, T. et al. Experimental demonstration of topological surface states protected by time-reversal symmetry. *Phys. Rev. Lett.* **103**, 266803 (2009).
14. Chen, Y. L. et al. Massive Dirac fermion on the surface of a magnetically doped topological insulator. *Science* **329**, 659–662 (2010).
15. Analytis, J. G. et al. Two-dimensional surface state in the quantum limit of a topological insulator. *Nat. Phys.* **6**, 960–964 (2010).
16. Alpichshev, Z. et al. STM Imaging of electronic waves on the surface of Bi_2Te_3: topologically protected surface states and hexagonal warping effects. *Phys. Rev. Lett.* **104**, 016401 (2010).
17. Fu, L. Topological crystalline insulators. *Phys. Rev. Lett.* **106**, 106802 (2011).
18. Hsieh, T. H. et al. Topological crystalline insulators in the SnTe material class. *Nat. Commun.* **3**, 982 (2012).
19. Yan, B. & Zhang, S.-C. Topological materials. *Rep. Prog. Phys.* **75**, 096501 (2012).
20. Müchler, L., Casper, F., Yan, B., Chadov, S. & Felser, C. Topological insulators and thermoelectric materials. *Phys. Status Solidi Rapid Res. Lett.* **7**, 91–100 (2013).
21. Ando, Y. & Fu, L. Topological crystalline insulators and topological superconductors: from concepts to materials. *Annu. Rev. Condens. Matter Phys.* **6**, 361–381 (2015).
22. Heremans, J. P., Cava, R. J. & Samarth, N. Tetradymites as thermoelectrics and topological insulators. *Nat. Rev. Mater.* **2**, 17049 (2017).
23. Tian, W., Yu, W., Shi, J. & Wang, Y. The property, preparation and application of topological insulators: a review. *Materials* **10**, 814 (2017).
24. Mishra, S., Satpathy, S. & Jepsen, O. Electronic structure and thermoelectric properties of bismuth telluride and bismuth selenide. *J. Phys. Condens. Matter* **9**, 461 (1997).
25. Xu, J.-L. et al. Ultrasensitive nonlinear absorption response of large-size topological insulator and application in low-threshold bulk pulsed lasers. *Sci. Rep.* **5**, 14856 (2015).
26. Yang, J. et al. Ultra-broadband flexible photodetector based on topological crystalline insulator SnTe with high responsivity. *Small* **14**, 1802598 (2018).
27. Hsieh, D. et al. Observation of unconventional quantum spin textures in topological insulators. *Science* **323**, 919–922 (2009).
28. Tian, J., Miotkowski, I., Hong, S. & Chen, Y. P. Electrical injection and detection of spin-polarized currents in topological insulator Bi_2Te_2Se. *Sci. Rep.* **5**, 14293 (2015).
29. Pesin, D. & MacDonald, A. H. Spintronics and pseudospintronics in graphene and topological insulators. *Nat. Mater.* **11**, 409–416 (2012).
30. Ando, Y. et al. Electrical detection of the spin polarization due to charge flow in the surface state of the topological insulator $Bi_{1.5}Sb_{0.5}Te_{1.7}Se_{1.3}$. *Nano Lett.* **14**, 6226–6230 (2014).
31. Tian, J., Hong, S., Miotkowski, I., Datta, S. & Chen, Y. P. Observation of current-induced, long-lived persistent spin polarization in a topological insulator: a rechargeable spin battery. *Sci. Adv.* **3**, e1602531 (2017).
32. Fan, Y. et al. Electric-field control of spin–orbit torque in a magnetically doped topological insulator. *Nat. Nanotechnol.* **11**, 352–359 (2016).
33. Kandala, A. et al. Growth and characterization of hybrid insulating ferromagnet–topological insulator heterostructure devices. *Appl. Phys. Lett.* **103**, 202409 (2013).
34. Yao, J., Shao, J., Wang, Y., Zhao, Z. & Yang, G. Ultra-broadband and high response of the Bi_2Te_3–Si heterojunction and its application as a photodetector at room temperature in harsh working environments. *Nanoscale* **7**, 12535–12541 (2015).
35. Xia, Y. et al. Observation of a large-gap topological-insulator class with a single Dirac cone on the surface. *Nat. Phys.* **5**, 398–402 (2009).
36. Chen, Y. L. et al. Experimental realization of a three-dimensional topological insulator, Bi_2Te_3. *Science* **325**, 178–181 (2009).
37. Arakane, T. et al. Tunable Dirac cone in the topological insulator $Bi_{2-x}Sb_xTe_{3-y}Se_y$. *Nat. Commun.* **3**, 636 (2012).
38. Nayak, J. et al. Temperature-induced modification of the Dirac cone in the tetradymite topological insulator Bi_2Te_2Se. *Phys. Rev. B* **98**, 075206 (2018).
39. Xu, Y. et al. Observation of topological surface state quantum Hall effect in an intrinsic three-dimensional topological insulator. *Nat. Phys.* **10**, 956–963 (2014).
40. Yoshimi, R. et al. Quantum Hall effect on top and bottom surface states of topological insulator $(Bi_{1-x}Sb_x)_2Te_3$ films. *Nat. Commun.* **6**, 6627 (2015).
41. Koirala, N. et al. Record surface state mobility and quantum Hall effect in topological insulator thin films via interface engineering. *Nano Lett.* **15**, 8245–8249 (2015).
42. Chang, C.-Z. et al. Experimental observation of the quantum anomalous Hall effect in a magnetic topological insulator. *Science* **340**, 167–170 (2013).
43. Nowack, K. C. et al. Imaging currents in HgTe quantum wells in the quantum spin Hall regime. *Nat. Mater.* **12**, 787–791 (2013).
44. Ma, E. Y. et al. Unexpected edge conduction in mercury telluride quantum wells under broken time-reversal symmetry. *Nat. Commun.* **6**, 7252 (2015).
45. Samarth, N. Quantum materials discovery from a synthesis perspective. *Nat. Mater.* **16**, 1068–1076 (2017).
46. Liu, Y. et al. Direct visualization of current-induced spin accumulation in topological insulators. *Nat. Commun.* **9**, 2492 (2018).
47. Di Pietro, P. et al. Observation of Dirac plasmons in a topological insulator. *Nat. Nanotechnol.* **8**, 556–560 (2013).
48. Bansal, N., Kim, Y. S., Brahlek, M., Edrey, E. & Oh, S. Thickness-independent transport channels in topological insulator Bi_2Se_3 thin films. *Phys. Rev. Lett.* **109**, 116804 (2012).
49. Shi, S. et al. Efficient charge-spin conversion and magnetization switching through the Rashba effect at topological-insulator/Ag interfaces. *Phys. Rev. B* **97**, 041115 (2018).
50. Belopolski, I. et al. A novel artificial condensed matter lattice and a new platform for one-dimensional topological phases. *Sci. Adv.* **3**, e1501692 (2017).
51. Zhang, J. et al. Band structure engineering in $(Bi_{1-x}Sb_x)_2Te_3$ ternary topological insulators. *Nat. Commun.* **2**, 574 (2011).
52. Qian, X., Liu, J., Fu, L. & Li, J. Quantum spin Hall effect in two-dimensional transition metal dichalcogenides. *Science* **346**, 1344–1347 (2014).
53. Fan, Y. et al. Unidirectional magneto-resistance in modulation-doped magnetic topological insulators. *Nano Lett.* **19**, 692–698 (2019).
54. Cen, C. et al. Nanoscale control of an interfacial metal–insulator transition at room temperature. *Nat. Mater.* **7**, 298–302 (2008).
55. Annadi, A. et al. Quantized ballistic transport of electrons and electron pairs in $LaAlO_3/SrTiO_3$ nanowires. *Nano Lett.* **18**, 4473–4481 (2018).
56. Peng, H. et al. Aharonov–Bohm interference in topological insulator nanoribbons. *Nat. Mater.* **9**, 225–229 (2009).
57. Hong, S. S., Zhang, Y., Cha, J. J., Qi, X.-L. & Cui, Y. One-dimensional helical transport in topological insulator nanowire interferometers. *Nano Lett.* **14**, 2815–2821 (2014).
58. Du, R. et al. Robustness of topological surface states against strong disorder observed in Bi_2Te_3 nanotubes. *Phys. Rev. B* **93**, 195402 (2016).
59. Jauregui, L. A., Pettes, M. T., Rokhinson, L. P., Shi, L. & Chen, Y. P. Magnetic field-induced helical mode and topological transitions in a topological insulator nanoribbon. *Nat. Nanotechnol.* **11**, 345–351 (2016).
60. Safdar, M. et al. Topological surface transport properties of single-crystalline SnTe nanowire. *Nano Lett.* **13**, 5344–5349 (2013).
61. Zhang, E. et al. Magnetotransport properties of Cd_3As_2 nanostructures. *ACS Nano* **9**, 8843–8850 (2015).
62. Majorana, E. Teoria simmetrica dell'elettrone e del positrone. *Nuovo Cimento* **14**, 171 (1937).
63. Alicea, J., Oreg, Y., Refael, G., von Oppen, F. & Fisher, M. P. A. Non-Abelian statistics and topological quantum information processing in 1D wire networks. *Nat. Phys.* **7**, 412–417 (2011).
64. Lutchyn, R. M. et al. Majorana zero modes in superconductor–semiconductor heterostructures. *Nat. Rev. Mater.* **3**, 52–68 (2018).
65. Kong, D. et al. Few-layer nanoplates of Bi_2Se_3 and Bi_2Te_3 with highly tunable chemical potential. *Nano Lett.* **10**, 2245–2250 (2010).
66. Hamdou, B., Gooth, J., Dorn, A., Pippel, E. & Nielsch, K. Aharonov–Bohm oscillations and weak antilocalization in topological insulator Sb_2Te_3 nanowires. *Appl. Phys. Lett.* **102**, 223110 (2013).
67. Purkayastha, A., Lupo, F., Kim, S., Borca-Tasciuc, T. & Ramanath, G. Low-temperature, template-free synthesis of single-crystal bismuth telluride nanorods. *Adv. Mater.* **18**, 496–500 (2006).
68. Xiao, F., Yoo, B., Lee, K. H. & Myung, N. V. Synthesis of Bi_2Te_3 nanotubes by galvanic displacement. *J. Am. Chem. Soc.* **129**, 10068–10069 (2007).
69. Jiang, Y. & Zhu, Y.-J. Bi_2Te_3 nanostructures prepared by microwave heating. *J. Cryst. Growth* **306**, 351–355 (2007).
70. Wang, W. et al. High-yield synthesis of single-crystalline antimony telluride hexagonal nanoplates using a solvothermal approach. *J. Am. Chem. Soc.* **127**, 13792–13793 (2005).
71. Kong, D. et al. Topological insulator nanowires and nanoribbons. *Nano Lett.* **10**, 329–333 (2010).

72. Kong, D. et al. Ambipolar field effect in the ternary topological insulator $(Bi_xSb_{1-x})_2Te_3$ by composition tuning. *Nat. Nanotechnol.* **6**, 705–709 (2011).
73. Cha, J. J. et al. Weak antilocalization in $Bi_2(Se_xTe_{1-x})_3$ nanoribbons and nanoplates. *Nano Lett.* **12**, 1107–1111 (2012).
74. Cha, J. J. et al. Magnetic doping and Kondo effect in Bi_2Se_3 nanoribbons. *Nano Lett.* **10**, 1076–1081 (2010).
75. Wang, Y. et al. Gate-controlled surface conduction in Na-doped Bi_2Te_3 topological insulator nanoplates. *Nano Lett.* **12**, 1170–1175 (2012).
76. Cheng, L. et al. High Curie temperature $Bi_{1.85}Mn_{0.15}Te_3$ nanoplates. *J. Am. Chem. Soc.* **134**, 18920–18923 (2012).
77. Hong, S. S., Cha, J. J., Kong, D. & Cui, Y. Ultra-low carrier concentration and surface-dominant transport in antimony-doped Bi_2Se_3 topological insulator nanoribbons. *Nat. Commun.* **3**, 757 (2012).
78. Dun, C. et al. Flexible n-type thermoelectric films based on Cu-doped Bi_2Se_3 nanoplate and polyvinylidene fluoride composite with decoupled Seebeck coefficient and electrical conductivity. *Nano Energy* **18**, 306–314 (2015).
79. Chen, Z.-G. et al. Paramagnetic Cu-doped Bi_2Te_3 nanoplates. *Appl. Phys. Lett.* **104**, 053105 (2014).
80. Senthil, T. Symmetry-protected topological phases of quantum matter. *Annu. Rev. Condens. Matter Phys.* **6**, 299–324 (2015).
81. Shen, J. et al. Synthesis of SnTe nanoplates with {100} and {100} surfaces. *Nano Lett.* **14**, 4183–4188 (2014).
82. Liu, X.-J., He, J. J. & Law, K. T. Demonstrating lattice symmetry protection in topological crystalline superconductors. *Phys. Rev. B* **90**, 235141 (2014).
83. Safdar, M., Wang, Q., Mirza, M., Wang, Z. & He, J. Crystal shape engineering of topological crystalline insulator SnTe microcrystals and nanowires with huge thermal activation energy gap. *Cryst. Growth Des.* **14**, 2502–2509 (2014).
84. Wang, Q. et al. Rational design of ultralarge $Pb_{1-x}Sn_xTe$ nanoplates for exploring crystalline symmetry-protected topological transport. *Adv. Mater.* **28**, 617–623 (2016).
85. Wang, Q. et al. Van der Waals epitaxial ultrathin two-dimensional nonlayered semiconductor for highly efficient flexible optoelectronic devices. *Nano Lett.* **15**, 1183–1189 (2015).
86. Wang, Q. et al. Van der Waals epitaxy and photoresponse of hexagonal tellurium nanoplates on flexible mica sheets. *ACS Nano* **8**, 7497–7505 (2014).
87. Wang, Q. et al. Topological crystalline insulator $Pb_{1-x}Sn_xSe$ nanowires with {100} facets. *Small* **11**, 2019–2025 (2015).
88. Safdar, M. et al. Weak antilocalization effect of topological crystalline insulator $Pb_{1-x}Sn_xTe$ nanowires with tunable composition and distinct {100} facets. *Nano Lett.* **15**, 2485–2490 (2015).
89. Shen, J., Xie, Y. & Cha, J. J. Revealing surface states in In-doped SnTe nanoplates with low bulk mobility. *Nano Lett.* **15**, 3827–3832 (2015).
90. Sasaki, S. & Ando, Y. Superconducting $Sn_{1-x}In_xTe$ nanoplates. *Cryst. Growth Des.* **15**, 2748–2752 (2015).
91. Shen, J., Woods, J. M., Xie, Y., Morales-Acosta, M. D. & Cha, J. J. Structural phase transition and carrier density tuning in $SnSe_xTe_{1-x}$ nanoplates. *Adv. Electron. Mater.* **2**, 1600144 (2016).
92. Xu, N. et al. Observation of Weyl nodes and Fermi arcs in tantalum phosphide. *Nat. Commun.* **7**, 11006 (2016).
93. Xu, S.-Y. et al. Experimental discovery of a topological Weyl semimetal state in TaP. *Sci. Adv.* **1**, e1501092 (2015).
94. Xu, S.-Y. et al. Discovery of a Weyl fermion state with Fermi arcs in niobium arsenide. *Nat. Phys.* **11**, 748–754 (2015).
95. Liu, Z. et al. Evolution of the Fermi surface of Weyl semimetals in the transition metal pnictide family. *Nat. Mater.* **15**, 27–31 (2016).
96. Zhou, L. et al. Large-area synthesis of high-quality uniform few-layer $MoTe_2$. *J. Am. Chem. Soc.* **137**, 11892–11895 (2015).
97. Naylor, C. H. et al. Monolayer single-crystal 1T′-$MoTe_2$ grown by chemical vapor deposition exhibits weak antilocalization effect. *Nano Lett.* **16**, 4297–4304 (2016).
98. Kwak, J. et al. Single-crystalline nanobelts composed of transition metal ditellurides. *Adv. Mater.* **30**, 1707260 (2018).
99. Naylor, C. H. et al. Large-area synthesis of high-quality monolayer 1T′-WTe_2 flakes. *2D Mater.* **4**, 021008 (2017).
100. Soluyanov, A. A. et al. Type-II Weyl semimetals. *Nature* **527**, 495–498 (2015).
101. Li, H. et al. Controlled synthesis of topological insulator nanoplate arrays on mica. *J. Am. Chem. Soc.* **134**, 6132–6135 (2012).
102. Roushan, P. et al. Topological surface states protected from backscattering by chiral spin texture. *Nature* **460**, 1106–1109 (2009).
103. Cho, S. et al. Aharonov–Bohm oscillations in a quasi-ballistic three-dimensional topological insulator nanowire. *Nat. Commun.* **6**, 7634 (2015).
104. Williams, J. R. et al. Unconventional Josephson effect in hybrid superconductor–topological insulator devices. *Phys. Rev. Lett.* **109**, 056803 (2012).
105. Mourik, V. et al. Signatures of Majorana fermions in hybrid superconductor–semiconductor nanowire devices. *Science* **336**, 1003–1007 (2012).
106. Sacépé, B. et al. Gate-tuned normal and superconducting transport at the surface of a topological insulator. *Nat. Commun.* **2**, 575 (2011).
107. Cho, S. et al. Symmetry protected Josephson supercurrents in three-dimensional topological insulators. *Nat. Commun.* **4**, 1689 (2013).
108. Wang, L.-X., Li, C.-Z., Yu, D.-P. & Liao, Z.-M. Aharonov–Bohm oscillations in Dirac semimetal Cd_3As_2 nanowires. *Nat. Commun.* **7**, 10769 (2016).
109. Keum, D. H. et al. Bandgap opening in few-layered monoclinic $MoTe_2$. *Nat. Phys.* **11**, 482–486 (2015).
110. Li, P. et al. Evidence for topological type-II Weyl semimetal WTe_2. *Nat. Commun.* **8**, 2150 (2017).
111. Cha, J. J., Koski, K. J. & Cui, Y. Topological insulator nanostructures. *Phys. Status Solidi Rapid Res. Lett.* **7**, 15–25 (2013).
112. Shen, J. & Cha, J. J. Topological crystalline insulator nanostructures. *Nanoscale* **6**, 14133–14140 (2014).
113. Kong, D., Koski, K. J., Cha, J. J., Hong, S. S. & Cui, Y. Ambipolar field effect in Sb-doped Bi_2Se_3 nanoplates by solvothermal synthesis. *Nano Lett.* **13**, 632–636 (2013).
114. Steinberg, H., Gardner, D. R., Lee, Y. S. & Jarillo-Herrero, P. Surface state transport and ambipolar electric field effect in Bi_2Se_3 nanodevices. *Nano Lett.* **10**, 5032–5036 (2010).
115. Hikami, S., Larkin, A. I. & Nagaoka, Y. Spin-orbit interaction and magnetoresistance in the two dimensional random system. *Prog. Theor. Phys.* **63**, 707–710 (1980).
116. Hamdou, B., Gooth, J., Dorn, A., Pippel, E. & Nielsch, K. Surface state dominated transport in topological insulator Bi_2Te_3 nanowires. *Appl. Phys. Lett.* **103**, 193107 (2013).
117. Ning, W. et al. One-dimensional weak antilocalization in single-crystal Bi_2Te_3 nanowires. *Sci. Rep.* **3**, 1564 (2013).
118. Cao, H. et al. Quantized Hall effect and Shubnikov–de Haas oscillations in highly doped Bi_2Se_3: evidence for layered transport of bulk carriers. *Phys. Rev. Lett.* **108**, 216803 (2012).
119. Zhang, Y., Tan, Y.-W., Stormer, H. L. & Kim, P. Experimental observation of the quantum Hall effect and Berry's phase in graphene. *Nature* **438**, 201–204 (2005).
120. Tang, H., Liang, D., Qiu, R. L. J. & Gao, X. P. A. Two-dimensional transport-induced linear magneto-resistance in topological insulator Bi_2Se_3 nanoribbons. *ACS Nano* **5**, 7510–7516 (2011).
121. McIver, J., Hsieh, D., Steinberg, H., Jarillo-Herrero, P. & Gedik, N. Control over topological insulator photocurrents with light polarization. *Nat. Nanotechnol.* **7**, 96–100 (2012).
122. Kong, D. et al. Rapid surface oxidation as a source of surface degradation factor for Bi_2Se_3. *ACS Nano* **5**, 4698–4703 (2011).
123. Liu, J., Duan, W. & Fu, L. Two types of surface states in topological crystalline insulators. *Phys. Rev. B* **88**, 241303 (2013).
124. Assaf, B. A. et al. Quantum coherent transport in SnTe topological crystalline insulator thin films. *Appl. Phys. Lett.* **105**, 102108 (2014).
125. Katayama, S. & Mills, D. Theory of anomalous resistivity associated with structural phase transitions in IV–VI compounds. *Phys. Rev. B* **22**, 336 (1980).
126. Kobayashi, K., Kato, Y., Katayama, Y. & Komatsubara, K. Carrier-concentration-dependent phase transition in SnTe. *Phys. Rev. Lett.* **37**, 772 (1976).
127. Kristoffel, N. & Konsin, P. Pseudo-Jahn–Teller effect and second order phase transitions in crystals. *Phys. Status Solidi* **21**, K39–K43 (1967).
128. Kumaravadivel, P. et al. Synthesis and superconductivity of In-doped SnTe nanostructures. *APL Mater.* **5**, 076110 (2017).
129. Atherton, S., Steele, B. & Sasaki, S. Unexpected Au alloying in tailoring In-doped SnTe nanostructures with gold nanoparticles. *Crystals* **7**, 78 (2017).
130. Xiong, J. et al. Evidence for the chiral anomaly in the Dirac semimetal Na_3Bi. *Science* **350**, 413–416 (2015).
131. Zhang, C. et al. Quantum Hall effect based on Weyl orbits in Cd_3As_2. *Nature* **565**, 331–336 (2019).
132. Moll, P. J. et al. Transport evidence for Fermi-arc-mediated chirality transfer in the Dirac semimetal Cd_3As_2. *Nature* **535**, 266–270 (2016).
133. Fatemi, V. et al. Electrically tunable low-density superconductivity in a monolayer topological insulator. *Science* **362**, 926–929 (2018).
134. Sajadi, E. et al. Gate-induced superconductivity in a monolayer topological insulator. *Science* **362**, 922–925 (2018).
135. Wu, S. et al. Observation of the quantum spin Hall effect up to 100 kelvin in a monolayer crystal. *Science* **359**, 76–79 (2018).
136. Hor, Y. S. et al. Superconductivity in $Cu_xBi_2Se_3$ and its implications for pairing in the undoped topological insulator. *Phys. Rev. Lett.* **104**, 057001 (2010).
137. Sasaki, S. et al. Topological superconductivity in $Cu_xBi_2Se_3$. *Phys. Rev. Lett.* **107**, 217001 (2011).
138. Liu, Z. et al. Superconductivity with topological surface state in $Sr_xBi_2Se_3$. *J. Am. Chem. Soc.* **137**, 10512–10515 (2015).
139. Zhao, L. et al. Emergent surface superconductivity in the topological insulator Sb_2Te_3. *Nat. Commun.* **6**, 8279 (2015).
140. Novak, M., Sasaki, S., Kriener, M., Segawa, K. & Ando, Y. Unusual nature of fully gapped superconductivity in In-doped SnTe. *Phys. Rev. B* **88**, 140502 (2013).
141. Sato, T. et al. Fermiology of the strongly spin-orbit coupled superconductor $Sn_{1-x}In_xTe$: implications for topological superconductivity. *Phys. Rev. Lett.* **110**, 206804 (2013).
142. Erickson, A. S., Chu, J. H., Toney, M. F., Geballe, T. H. & Fisher, I. R. Enhanced superconducting pairing interaction in indium-doped tin telluride. *Phys. Rev. B* **79**, 024520 (2009).
143. Kang, D. et al. Superconductivity emerging from a suppressed large magnetoresistant state in tungsten ditelluride. *Nat. Commun.* **6**, 7804 (2015).
144. Pan, X.-C. et al. Pressure-driven dome-shaped superconductivity and electronic structural evolution in tungsten ditelluride. *Nat. Commun.* **6**, 7805 (2015).
145. Qi, Y. et al. Superconductivity in Weyl semimetal candidate $MoTe_2$. *Nat. Commun.* **7**, 11038 (2016).
146. Chen, F. C. et al. Superconductivity enhancement in the S-doped Weyl semimetal candidate $MoTe_2$. *Appl. Phys. Lett.* **108**, 162601 (2016).
147. Sasaki, S. et al. Odd-parity pairing and topological superconductivity in a strongly spin–orbit coupled semiconductor. *Phys. Rev. Lett.* **109**, 217004 (2012).
148. Koski, K. J. et al. Chemical intercalation of zerovalent metals into 2D layered Bi_2Se_3 nanoribbons. *J. Am. Chem. Soc.* **134**, 13773–13779 (2012).
149. Koski, K. J. et al. High-density chemical intercalation of zero-valent copper into Bi_2Se_3 nanoribbons. *J. Am. Chem. Soc.* **134**, 7584–7587 (2012).
150. Kitaev, A. Y. Unpaired Majorana fermions in quantum wires. *Phys. Usp.* **44**, 131 (2001).
151. Read, N. & Green, D. Paired states of fermions in two dimensions with breaking of parity and time-reversal symmetries and the fractional quantum Hall effect. *Phys. Rev. B* **61**, 10267–10297 (2000).
152. Ivanov, D. A. Non-Abelian statistics of Half-quantum vortices in *p*-wave superconductors. *Phys. Rev. Lett.* **86**, 268–271 (2001).
153. Snyder, R. et al. Weak-link Josephson junctions made from topological crystalline insulators. *Phys. Rev. Lett.* **121**, 097701 (2018).
154. Cook, A. M., Vazifeh, M. M. & Franz, M. Stability of Majorana fermions in proximity-coupled topological insulator nanowires. *Phys. Rev. B* **86**, 155431 (2012).
155. Nomura, K., Koshino, M. & Ryu, S. Topological delocalization of two-dimensional massless Dirac fermions. *Phys. Rev. Lett.* **99**, 146806 (2007).
156. Bardarson, J. H., Brouwer, P. W. & Moore, J. E. Aharonov–Bohm oscillations in disordered topological insulator nanowires. *Phys. Rev. Lett.* **105**, 156803 (2010).
157. Huang, Y. et al. Metamorphosis of Andreev bound states into Majorana bound states in pristine nanowires. *Phys. Rev. B* **98**, 144511 (2018).

158. Estrada Saldaña, J. C. et al. Split-channel ballistic transport in an InSb nanowire. *Nano Lett.* **18**, 2282–2287 (2018).
159. Potter, A. C. & Lee, P. A. Engineering a $p + ip$ superconductor: comparison of topological insulator and Rashba spin–orbit-coupled materials. *Phys. Rev. B* **83**, 184520 (2011).
160. Liu, P. et al. Dislocation-driven SnTe surface defects during chemical vapor deposition growth. *J. Phys. Chem. Solids* https://doi.org/10.1016/j.jpcs.2017.12.016 (2017).
161. Kim, B. J. et al. Kinetics of individual nucleation events observed in nanoscale vapor–liquid–solid growth. *Science* **322**, 1070–1073 (2008).
162. Hannon, J. B., Kodambaka, S., Ross, F. M. & Tromp, R. M. The influence of the surface migration of gold on the growth of silicon nanowires. *Nature* **440**, 69–71 (2006).
163. Oh, S. H. et al. Oscillatory mass transport in vapor–liquid–solid growth of sapphire nanowires. *Science* **330**, 489–493 (2010).
164. Jacobsson, D. et al. Interface dynamics and crystal phase switching in GaAs nanowires. *Nature* **531**, 317–322 (2016).
165. Bhimanapati, G. R. et al. Recent advances in two-dimensional materials beyond graphene. *ACS Nano* **9**, 11509–11539 (2015).
166. Govind Rajan, A., Warner, J. H., Blankschtein, D. & Strano, M. S. Generalized mechanistic model for the chemical vapor deposition of 2D transition metal dichalcogenide monolayers. *ACS Nano* **10**, 4330–4344 (2016).
167. Shi, Y., Li, H. & Li, L.-J. Recent advances in controlled synthesis of two-dimensional transition metal dichalcogenides via vapour deposition techniques. *Chem. Soc. Rev.* **44**, 2744–2756 (2015).
168. Hong, S. et al. Chemical vapor deposition synthesis of MoS_2 layers from the direct sulfidation of MoO_3 surfaces using reactive molecular dynamics simulations. *J. Phys. Chem. C.* **122**, 7494–7503 (2018).
169. Deringer, V. L. & Dronskowski, R. Stability of pristine and defective SnTe surfaces from first principles. *ChemPhysChem* **14**, 3108–3111 (2013).
170. Li, Z. et al. Single crystalline nanostructures of topological crystalline insulator SnTe with distinct facets and morphologies. *Nano Lett.* **13**, 5443–5448 (2013).
171. Zhang, J., Sun, J., Li, Y., Shi, F. & Cui, Y. Electrochemical control of copper intercalation into nanoscale Bi_2Se_3. *Nano Lett.* **17**, 1741–1747 (2017).
172. Zhang, T. et al. Catalogue of topological electronic materials. *Nature* **566**, 475–479 (2019).
173. Vergniory, M. G. et al. A complete catalogue of high-quality topological materials. *Nature* **566**, 480–485 (2019).
174. Tang, F., Po, H. C., Vishwanath, A. & Wan, X. Comprehensive search for topological materials using symmetry indicators. *Nature* **566**, 486–489 (2019).
175. Sochnikov, I. et al. Nonsinusoidal current–phase relationship in Josephson junctions from the 3D topological insulator HgTe. *Phys. Rev. Lett.* **114**, 066801 (2015).
176. Wang, A.-Q. et al. 4π-periodic supercurrent from surface states in Cd_3As_2 nanowire-based Josephson junctions. *Phys. Rev. Lett.* **121**, 237701 (2018).
177. Furusaki, A. Josephson current carried by Andreev levels in superconducting quantum point contacts. *Superlattices Microstruct.* **25**, 809–818 (1999).
178. Barone, A. & Paterno, G. Physics and Applications of the Josephson Effect (Wiley, 1982).
179. Grbic, B. et al. Aharonov–Bohm oscillations in the presence of strong spin–orbit interactions. *Phys. Rev. Lett.* **99**, 176803 (2007).
180. Akhmerov, A. R., Dahlhaus, J. P., Hassler, F., Wimmer, M. & Beenakker, C. W. J. Quantized conductance at the Majorana phase transition in a disordered superconducting wire. *Phys. Rev. Lett.* **106**, 057001 (2011).
181. Banerjee, M. et al. Observation of half-integer thermal Hall conductance. *Nature* **559**, 205–210 (2018).
182. Gibney, E. Thousands of exotic 'topological' materials discovered through sweeping search. *Nature* **560**, 151–152 (2018).
183. Wagner, R. S. & Ellis, W. C. Vapor–liquid–solid mechanism of single crystal growth. *Appl. Phys. Lett.* **4**, 89–90 (1964).
184. Cui, Y., Lauhon, L. J., Gudiksen, M. S., Wang, J. & Lieber, C. M. Diameter-controlled synthesis of single-crystal silicon nanowires. *Appl. Phys. Lett.* **78**, 2214–2216 (2001).
185. Gudiksen, M. S., Lauhon, L. J., Wang, J., Smith, D. C. & Lieber, C. M. Growth of nanowire superlattice structures for nanoscale photonics and electronics. *Nature* **415**, 617–620 (2002).
186. Lauhon, L. J., Gudiksen, M. S., Wang, D. & Lieber, C. M. Epitaxial core–shell and core–multishell nanowire heterostructures. *Nature* **420**, 57–61 (2002).
187. Tang, J., Huo, Z., Brittman, S., Gao, H. & Yang, P. Solution-processed core–shell nanowires for efficient photovoltaic cells. *Nat. Nanotechnol.* **6**, 568–572 (2011).
188. Zhou, J. et al. A library of atomically thin metal chalcogenides. *Nature* **556**, 355–359 (2018).
189. Shi, Y. et al. Synthesis of few-layer hexagonal boron nitride thin film by chemical vapor deposition. *Nano Lett.* **10**, 4134–4139 (2010).
190. Alicea, J. New directions in the pursuit of Majorana fermions in solid state systems. *Rep. Prog. Phys.* **75**, 076501 (2012).
191. Zhang, K. et al. Controllable synthesis and magnetotransport properties of Cd_3As_2 Dirac semimetal nanostructures. *RSC Adv.* **7**, 17689–17696 (2017).
192. Kim, D. et al. Intrinsic electron–phonon resistivity of Bi_2Se_3 in the topological regime. *Phys. Rev. Lett.* **109**, 166801 (2012).
193. Fong, K. C. & Schwab, K. Ultrasensitive and wide-bandwidth thermal measurements of graphene at low temperatures. *Phys. Rev. X* **2**, 031006 (2012).

Acknowledgements
P.L. is supported by the US National Science Foundation (NSF) DMR 1743896. J.R.W. acknowledges support from NSF DMR 1743913. J.J.C. acknowledges support from the US Department of Energy DE-SC0014476.

Author contributions
All authors contributed to the discussion of content and writing of the manuscript.

Competing interests
The authors declare no competing interests.